

Is the dark-matter halo spin a predictor of galaxy spin and size?

Fangzhou Jiang^{1*}, Avishai Dekel^{1,2†}, Omer Kneller¹, Sharon Lapiner¹, Daniel Ceverino³, Joel R. Primack⁴, Sandra M. Faber⁵, Andrea Macciò^{6,7}, Aaron Dutton⁶, Shy Genel^{8,9}, Rachel S. Somerville^{8,10}

¹Center for Astrophysics and Planetary Science, Racah Institute of Physics, The Hebrew University, Jerusalem 91904, Israel

²SCIPP, University of California, Santa Cruz, CA 95064, USA

³Universität Heidelberg, Zentrum für Astronomie, Institut für Theoretische Astrophysik, Albert-Ueberle-Str. 2, 69120 Heidelberg, Germany

⁴Department of Physics, University of California, Santa Cruz, CA 95064, USA

⁵Department of Astronomy, University of California, Santa Cruz, CA 95064, USA

⁶New York University Abu Dhabi, PO Box 129188, Abu Dhabi, United Arab Emirates

⁷Max Planck Institute für Astronomie, Königstuhl 17, D-69117 Heidelberg, Germany

⁸Center for Computational Astrophysics, Flatiron Institute, 162 Fifth Avenue, New York, NY 10010, USA

⁹Columbia Astrophysics Laboratory, Columbia University, 550 West 120th Street, New York, NY 10027, USA

¹⁰Department of Physics and Astronomy, Rutgers, The State University of New Jersey, 136 Frelinghuysen Rd, Piscataway, NJ 08854, USA

23 April 2018

ABSTRACT

The similarity between the distributions of spins for galaxies (λ_{gal}) and for dark-matter haloes (λ_{halo}), indicated both by simulations and observations, is naively interpreted as a one-to-one correlation between the spins of a galaxy and its host halo. This is used to predict galaxy sizes in semi-analytic models via $R_e \simeq \lambda_{\text{halo}} R_{\text{vir}}$, where R_e is the half-mass radius of the galaxy and R_{vir} is the halo radius. Utilizing two different suites of zoom-in cosmological simulations, we find that λ_{gal} and the λ_{halo} of its host halo are in fact only barely correlated, especially at $z \geq 1$. A general smearing of this correlation is expected based on the different spin histories, where the more recently accreted baryons through streams gain and then lose significant angular momentum compared to the gradually accumulated dark matter. Expecting the spins of baryons and dark matter to be correlated at accretion into R_{vir} , the null correlation at the end reflects an anti-correlation between $\lambda_{\text{gal}}/\lambda_{\text{halo}}$ and λ_{halo} , which can partly arise from mergers and a compact star-forming phase that many galaxies undergo. On the other hand, the halo and galaxy spin vectors tend to be aligned, with a median $\cos \theta = 0.6$ – 0.7 between galaxy and halo, consistent with instreaming within a preferred plane. The galaxy spin is better correlated with the spin of the inner halo, but this largely reflects the effect of the baryons on the halo. Following the null spin correlation, λ_{halo} is not a useful proxy for R_e . While our simulations reproduce a general relation of the sort $R_e = AR_{\text{vir}}$, in agreement with observational estimates, the relation becomes tighter with $A = 0.02(c/10)^{-0.7}$, where c is the halo concentration, which in turn introduces a dependence on mass and redshift.

Key words: dark matter — galaxies: evolution — galaxies: formation — galaxies: haloes

1 INTRODUCTION

In the standard paradigm of hierarchical structure formation, the angular momentum (AM) growth of a dark matter protohalo is driven by the large-scale gravitational tidal torque until maximum expansion. This

* E-mail: fangzhou.jiang@huji.ac.il

† E-mail: dekel@huji.ac.il

“tidal torque theory (TTT)” (e.g., Doroshkevich 1970; White 1984) has been shown to agree well with the predictions from cosmological N -body simulations (e.g., Porciani, Dekel & Hoffman 2002a,b). The AM of a halo is often characterized using the dimensionless spin parameter (Bullock et al. 2001):

$$\lambda = \frac{j}{\sqrt{2}V_{\text{vir}}R_{\text{vir}}} \quad (1)$$

where $j = J/M$ is the specific angular momentum (sAM) and where R_{vir} and V_{vir} are the virial radius and velocity of the halo.¹ The spin parameter as defined in eq. (1) can refer to any part of the halo, and to any component of the galaxy inside the halo, such as the gas and/or stars in the disc and/or the whole galaxy, using the specific angular momentum of the component of interest.

Galaxies form as cold gas condenses within the potential wells of dark matter haloes (White & Rees 1978; Blumenthal et al. 1984). Since the baryons and the dark matter have similar spatial distributions in the cosmic web, they are expected to gain comparable amount of sAM through the large-scale tidal torques. It used to be commonly assumed that the AM of the gas is conserved during the collapse, such that the galactic disc is expected to have a similar spin to that of its hosting halo $\lambda_{\text{gal}} \simeq \lambda_{\text{halo}}$ (Fall & Efstathiou 1980; Mo, Mao & White 1998; Bullock et al. 2001). In addition, the rotation curves of galaxies are close to flat, so for disc galaxies the rotation speed at some characteristic radius of the galaxy, V_{rot} , is comparable to the virial velocity V_{vir} . These establish a link between the characteristic radius of the galaxy and the virial radius of the halo. The sAM of a galaxy can be written as

$$j_{\text{gal}} \simeq R_{\text{e}}V_{\text{rot}}, \quad (2)$$

where R_{e} is the 3D half stellar mass radius of a galaxy.² The radius of the galaxy can be expressed as

$$\begin{aligned} R_{\text{e}} &\simeq \frac{j_{\text{gal}}}{j_{\text{halo}}} \frac{j_{\text{halo}}}{R_{\text{vir}}V_{\text{vir}}} \frac{V_{\text{vir}}}{V_{\text{rot}}} R_{\text{vir}} \\ &= f_j \lambda_{\text{halo}} R_{\text{vir}}. \end{aligned} \quad (3)$$

¹ Peebles (1969) originally defined the spin parameter for dark matter haloes as $\lambda = J|E|^{1/2}G^{-1}M^{-5/2}$, where J is the magnitude of the total dark-matter AM within the virial radius; M is the virial mass; and E is the total energy of the halo. Calculating the total energy E is computationally expensive, and the potential energy is not uniquely defined, hindering practical use of the definition. For smooth spherical haloes with all particles on circular orbits, the two definitions are linked via $\lambda_{\text{Peebles}} = \lambda_{\text{Bullock}}f_c^{-1/2}$, with f_c measuring the deviation of E from that of a singular isothermal sphere. The Bullock et al. definition enables one to compare the sAM of different components in a halo; while the Peebles definition can only be used considering all the mass inside a halo.

² The more familiar form of eq. (2) in the literature (e.g., Mo, Mao & White 1998) is, for exponential discs,

$$j_{\text{d}} = 2R_{\text{d}}V_{\text{c}},$$

where j_{d} is the sAM of the disc, R_{d} is the scale radius, and the rotation curve is flat at the level V_{c} . Here we opt for a more general expression. For exponential discs, $R_{\text{e}} \approx 1.68R_{\text{d}}$.

Here the factor $f_j \equiv \lambda_{\text{gal}}/\lambda_{\text{halo}}$, with λ_{gal} denoting $j_{\text{gal}}/(\sqrt{2}R_{\text{vir}}V_{\text{vir}})$, is taken as unity if the gas sAM is assumed to be conserved. This is adopted in most semi-analytic models of galaxy formation (e.g., Somerville et al. 2008; Guo et al. 2011; Benson 2012) when trying to predict disc sizes.

Cosmological N -body simulations show that halo spin follows log-normal distributions with a median of $\langle \lambda_{\text{halo}} \rangle \simeq 0.035$ and a standard deviation of $\sigma_{\log_{10} \lambda_{\text{halo}}} \simeq 0.25$ (e.g., Bullock et al. 2001, Bett et al. 2007). Hydrocosmological simulations show that λ_{gal} and λ_{halo} follow similar, log-normal distributions³. For example, the spin of gas within $0.1R_{\text{vir}}$ has a median value of ~ 0.04 and a standard deviation of ~ 0.25 dex (e.g., Danovich et al. 2015). Observed star-forming disc galaxies in the redshift range $z = 0.5$ -3 indicate a similar result (Burkert et al. 2016). The spin parameters of the discs were evaluated using their sAM based on measured H_{α} kinematics and normalized by the halo virial velocities and radii inferred from the kinematics and stellar mass. This study found that λ_{gas} obeys a log-normal distribution similar to those found for λ_{halo} (and λ_{gas}) in simulations.

At face value, the similarity between the distributions $P(\lambda_{\text{gal}})$ and $P(\lambda_{\text{halo}})$ may naively suggest that λ_{gal} of a given galaxy reflects λ_{halo} of the host halo. However, one should note that the two spin parameters, λ_{gal} and λ_{halo} , are quantities that refer to different spatial and temporal scales – the former mostly represents the sAM of the *inner* region and of recently arrived gas, while the latter represents the sAM of dark matter within the *whole* virial radius and is an integral over accretion throughout history. Generally, mass accreted more recently into the halo has higher sAM than the mass accreted earlier. For example, at the virial radius of a halo, the spin parameter of the dark matter and cold gas streams are of the order of 0.1-0.2 in simulations (Danovich et al. 2015), significantly higher than the spin of the overall halo. Therefore, the fact that the distributions of λ_{gal} and λ_{halo} are similar, actually hints against AM conservation.

Danovich et al. (2015) used cosmological simulations to study the evolution of gas sAM as gas streams from the cosmic web and feeds high- z galaxies. They described this evolution in four stages, as summarized in a cartoon in their Figure 20. They first revealed that outside the haloes, since the gas streams are thinner than the dark matter streams, they have higher quadrupole moments of the inertia tensor. Therefore, upon entering R_{vir} , the sAM of cold gas is highly correlated to, but ~ 1.5 times higher than, the sAM of the incoming dark matter. Inside R_{vir} , gas first maintains its AM in the outer halo while the incoming dark matter mixes with the existing halo of lower spin; then instreaming gas loses AM due to dissipation and torques from the inner galactic disc. Finally, torques and mass exchanges within the gaseous discs cause further changes

³ though there are differences between the distributions of spins of the different components of the galaxy

in the disc sAM. That is, overall, the gas gains and loses sAM with respect to the dark matter at different stages due to various mechanisms. Any mechanism that causes AM exchange or difference between the inner and outer parts of a halo, or any time variation of the AM supply in the cosmic web, can cause f_j to deviate from unity. Since these processes differ in strength from galaxy to galaxy and from time to time, f_j is expected to be stochastic, and the initial tight correlation between the sAM of incoming gas and dark matter is expected to be weakened or possibly smeared out. If f_j is stochastic or it is anti-correlated with λ_{halo} , the simple recipe for galaxy size as given by eq. (3) is problematic.

Kravtsov (2013) compiled a sample of nearby galaxies of mixed morphologies and inferred the relation between galaxy size and halo virial radius using abundance matching. He found that the data are scattered about a linear relation, $R_e \simeq AR_{\text{vir}}$, with $A = 0.015$ on average, and a scatter $\sigma_{\log A} \approx 0.25\text{dex}$. Interestingly, not only the median of the proportionality factor is of the order of what is expected for λ_{halo} , but also the scatter is similar to $\sigma_{\log \lambda_{\text{halo}}}$. Huang et al. (2017) and Somerville et al. (2018) extended the study of the kind of Kravtsov (2013) to $z = 0-3$. They confirmed the form of the linear relation, but reported slightly larger proportionality factors, with noticeable dependences on redshift. Somerville et al. (2018) showed in detail that the dispersion in the conditional size distribution in stellar mass bins is in excellent agreement with the simple ansatz $R_e \propto \lambda_{\text{halo}} R_{\text{vir}}$. However, as they point out, this does not prove that there is a strong one-to-one correlation between R_e and $\lambda_{\text{halo}} R_{\text{vir}}$. Given that λ_{halo} is expected to be almost constant over time and as a function of mass, the dependence of the proportionality factor on mass and redshift hints that other parameters in addition to λ_{halo} must play a role in determining galaxy size.

These concerns cast doubt on the simple assumptions of a strong one-to-one correlation between the spins of a galaxy and its host halo, and the role of halo spin in determining the galaxy size. This motivates us to examine these issues directly in cosmological hydrodynamical simulations. We use two suites of simulations with very different subgrid physics for this study. If no correlation between λ_{gal} and λ_{halo} is found, we will look for a revised recipe for predicting galaxy size in semi-analytic models.

The outline of this paper is as follows. In §2, we describe the simulations. In §3, we compare the distributions of spin of different components – cold gas, stars, and dark matter halo. In §4, we characterize the correlations between galaxy spin and halo spin. In §5, we present the correlations between gas spin and stellar spin. In §6, we explore the possible effects of wet compaction (a compact star forming phase that many galaxies undergo at high- z) and mergers on the $\lambda_{\text{gal}}-\lambda_{\text{halo}}$ correlation (or the lack thereof). In §7, we study the relation between galaxy size and halo virial radius. In §8, we compare our results to previous studies. In §9, we summarize our conclusions.

2 METHOD

In this study, we use two suites of zoom-in hydro-cosmological simulations, VELA and NIHAO, of different hydro-gravitational solver, resolution and different recipes for cooling, star formation, and stellar feedback.

2.1 VELA

VELA is a suite of zoom-in hydro-cosmological simulations of 34 moderately massive central galaxies. It utilizes the Adaptive Refinement Tree (ART) code (Kravtsov, Klypin & Khokhlov 1997; Kravtsov 2003), which follows the evolution of a gravitating N -body system and the Eulerian gas dynamics using an adaptive mesh. At the subgrid level, the code incorporates the key physical processes relevant for galaxy formation, including gas cooling by atomic hydrogen and helium as well as by metals and molecular hydrogen, photoionization heating by the UV background with partial self-shielding, star formation, stellar mass-loss, metal enrichment of the interstellar medium, and stellar feedback.

Star formation is stochastic in cells with gas temperature $T < 10^4$ K and densities $n_{\text{H}} > 1 \text{ cm}^{-3}$, at a rate consistent with the Kennicutt-Schmidt law (Kennicutt 1998). Supernovae and stellar winds are implemented by local injection of thermal energy at a constant rate, as in Ceverino & Klypin (2009), Ceverino, Dekel & Bournaud (2010), and Ceverino et al. (2012). Radiative stellar feedback is implemented with no significant infrared trapping, motivated by Dekel & Krumholz (2013), as described in Ceverino et al. (2014).

The simulation adopts the Wilkinson Microwave Anisotropy Probe 5 cosmological parameters ($\Omega_{\text{m}} = 0.27$, $\Omega_{\Lambda} = 0.73$, $\Omega_{\text{b}} = 0.045$, $h = 0.7$, $\sigma_8 = 0.82$) (Dunkley et al. 2009). The dark matter particle mass is $8.3 \times 10^4 M_{\odot}$, in the zoom-in region, and star particles have a minimum mass of $10^3 M_{\odot}$. The AMR cells are refined to a minimum size in the range 17-35 pc at all times in the dense regions. The force resolution is two grid cells, as required for computing the gradient of the gravitational potential. Each cell is split into eight cells once it contains a mass in stars and dark matter higher than $2.6 \times 10^5 M_{\odot}$, equivalent to three dark matter particles, or once it contains a gas mass higher than $1.5 \times 10^6 M_{\odot}$. The output timesteps that are analyzed are uniform in scale factor, with $\Delta a = 0.01$.

Among the 34 galaxies, 28 galaxies reach $z = 2$, with the majority reaching $z = 1$ and three of them reaching $z = 0.8$. The VELA galaxies are selected to be systems that, at $z = 1$, show no on-going major mergers, and are in the mass⁴ range of $M_{\text{vir}} = 2 \times 10^{11} - 2 \times 10^{12} M_{\odot}$, about a median of $4.6 \times 10^{11} M_{\odot}$. At $z = 2$,

⁴ Throughout the paper, halo mass is defined as the total mass within a sphere of radius R_{vir} that encompasses an overdensity of $\Delta_{\text{vir}}(z)$ times the critical density of the Universe (Bryan & Norman 1998).

the sample span the halo mass range of $(1-9) \times 10^{11} M_\odot$, and the stellar mass range of $(0.2-5.7) \times 10^{10} M_\odot$. If they were to evolve to $z = 0$, their mass range would bracket the Milky-Way mass. More details concerning the simulations are presented in Ceverino et al. (2014) and Zolotov et al. (2015).

2.2 NIHAO

We also use a subset of the Numerical Investigation of a Hundred Astrophysical Objects (NIHAO) project (Wang et al. 2015), consisting of 13 central galaxies that are Milky-Way sized or slightly more massive at $z=0$ [$M_{\text{vir}} = 7 \times 10^{11} - 3 \times 10^{12} M_\odot$], evolved using the SPH code Gasoline 2.0 (Wadsley, Keller & Quinn 2017). The code includes a subgrid model for turbulent mixing of metals and energy (Wadsley, Veeravalli & Couchman 2008), ultraviolet heating, ionization and metal cooling (Shen, Wadsley & Stinson 2010). Star formation and feedback follows the model used in the MaGICC simulations (Stinson et al. 2013), adopting a threshold for star formation of $n_{\text{H}} > 10.3 \text{ cm}^{-3}$. Stars feed energy back into the interstellar medium via blast-wave supernova feedback (Stinson et al. 2006) and early stellar feedback from massive stars.

The simulations are run in a flat Λ CDM cosmology with parameters from the Planck Collaboration et al. (2016) ($\Omega_{\text{m}} = 0.3175$, $\Omega_{\Lambda} = 0.6824$, $\Omega_{\text{b}} = 0.0490$, $h = 0.671$, $\sigma_8 = 0.8344$, $n = 0.9624$). Particle masses and force softenings are chosen to resolve the mass profile to below 1 per cent of the virial radius at all masses, ensuring that galaxy half-light radii are well resolved. For the 13 galaxies that we use, the particle mass is $1.735 \times 10^6 M_\odot$ for dark matter, and $3.166 \times 10^5 M_\odot$ for gas. The force softening length is 931.4pc for dark matter, and 397.9pc for baryons (co-moving). The output is uniform in cosmic time, with $\Delta t \simeq 215 \text{ Myr}$, approximately $\Delta a \simeq 0.014$ at $z \sim 1$.

2.3 Comments

The NIHAO galaxies reach $z = 0$, while more than half of the VELA galaxies reach $z = 1$, some reaching $z = 0.8$. Both suites consist of central galaxies, selected to be far from larger neighbours throughout their assembly history, and would be $\sim L_*$ or sub- L_* galaxies at $z = 0$, if left evolving in isolation.

In what follows, in order to probe potential redshift dependence, we bin the snapshots into three redshift ranges, $z = 0-0.8$, $0.8-2$, and $2-7$. To achieve better statistics, we consider *each galaxy at each snapshot* as an *independent* measurement. The median halo masses of the NIHAO snapshots are $\log(M_{\text{vir}}/M_\odot) = 11.82^{+0.21}_{-0.17}$, $11.59^{+0.29}_{-0.27}$, and $10.86^{+0.49}_{-0.43}$, in the three redshift ranges, respectively. Here the upper and lower limits indicate the 16th and 84th percentiles. The median halo masses of the VELA snapshots are $\log(M_{\text{vir}}/M_\odot) = 11.51^{+0.32}_{-0.25}$ and $10.99^{+0.45}_{-0.66}$ respectively, for $z = 0.8-2$, and $2-7$, respectively.

The two suites differ in many subgrid recipes, and

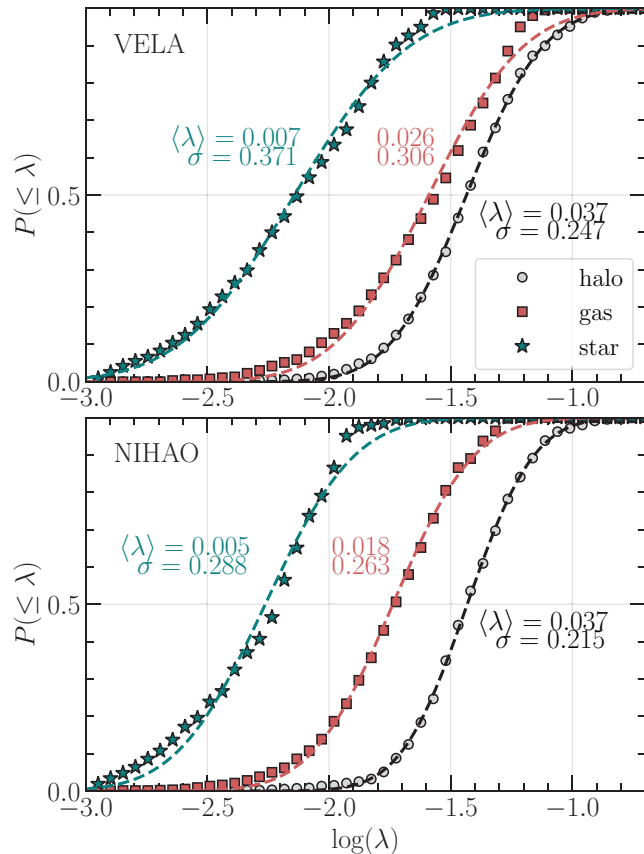


Figure 1. Cumulative distributions of the spin for host halo (within R_{vir}), cold gas (within $0.1R_{\text{vir}}$), and stars (within $0.1R_{\text{vir}}$) of the VELA (upper) and NIHAO (lower) simulations. The lines represent the best-fit log-normal distributions. λ_{gas} has a mean value slightly lower than λ_{halo} , and exhibits a marginally larger scatter, while λ_{star} is much lower than the other components and follows a much broader distribution. The NIHAO λ_{star} and λ_{halo} distributions are similar to those of VELA; while λ_{gas} in NIHAO is 0.15 dex lower.

in particular in numerical resolution and in the implementation of stellar feedback. The VELA simulations have relatively weak stellar feedback. The stellar-to-halo mass ratio in the VELA simulations is in ballpark agreement (considering the scatter in these relations) with the results of abundance matching relations from Behroozi, Wechsler & Conroy (2013) and Moster, Naab & White (2013). The stellar feedback of the NIHAO simulation is much stronger than VELA, and is tuned to match the $z = 0$ stellar mass versus halo mass relation from abundance matching. The two simulations are therefore complementary in terms of revealing potential dependence of the results on the feedback strength. Neither VELA or NIHAO has included AGNs. The effects of AGNs may start to become important for L_* -galaxies. The most massive end of our sample may be affected and therefore should be taken with caution.

The NIHAO galaxies are mostly on the star formation main sequence, while the VELA simulations exhibit more diverse sSFR. Very few galaxies in our sample are completely quenched. There have been a plethora of

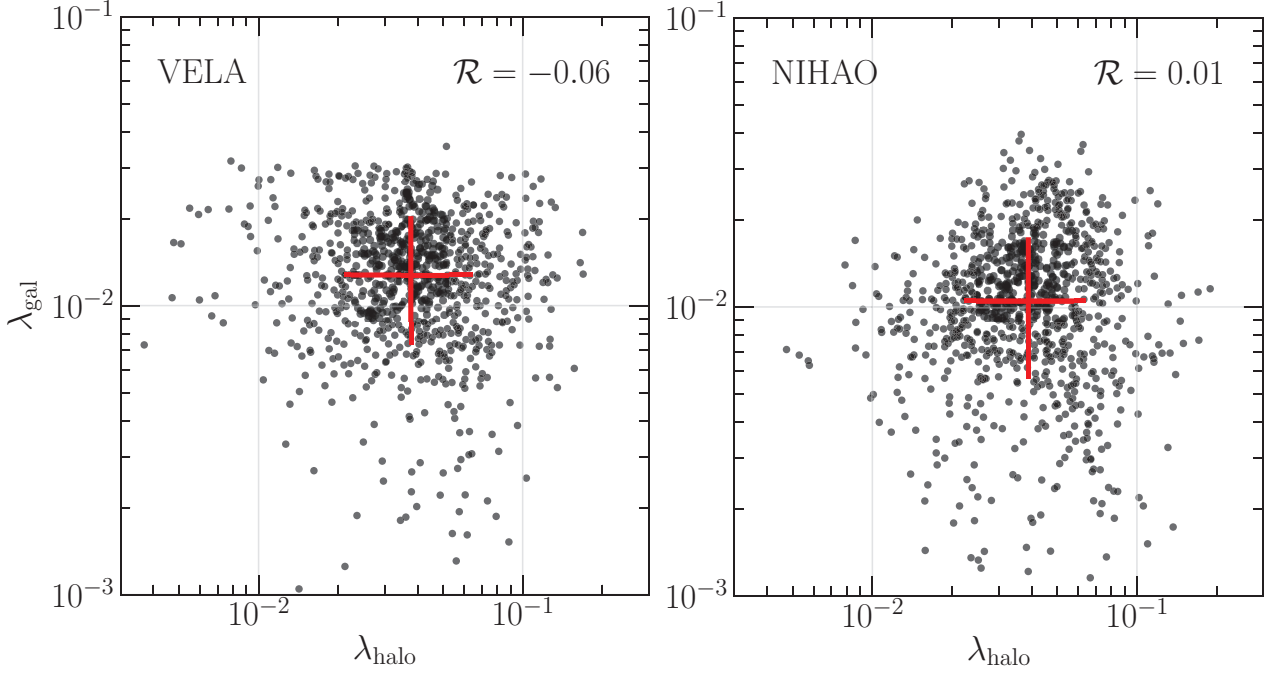


Figure 2. The spin of a galaxy (stars+cold gas within $0.1R_{\text{vir}}$) versus the spin of its host halo (DM within R_{vir}), for the VELA (*left*) and NIHAO (*right*) simulations. Each dot is a *galaxy at one snapshot*. Here we have corrected for systematic dependence on halo mass or redshift (see text). The cross marks the median and the 16th and 84th percentiles. The Pearson correlation coefficient \mathcal{R} is quoted at the upper right corner. In both simulations, there is negligible correlation between λ_{gal} and λ_{halo} .

studies discussing the correlation between morphology and angular momentum loss, and this is *not* the focus of this paper – we generally do not distinguish early-type and late-type galaxies in the following, unless there is a significant morphology-dependence in the results. We verify though that our main results hold if we only use the galaxies on or off the main sequence.

2.4 Measuring Spin

Galaxy centers are defined as follows. For the VELA simulations, we identify the cell of the highest baryonic density, draw a sphere of 1kpc around it, and take the center-of-mass (CoM) of the stars in the 1kpc-sphere as the center position, \mathbf{r}_0 . The CoM velocity of these stars is taken as the bulk velocity, \mathbf{v}_0 , which is then used to define the rest frame for calculating the AM.

For the NIHAO galaxies, we take the center of the host halo as given by the AHF halo catalog (Knollmann & Knebe 2009) as an initial guess, and run a shrinking-sphere algorithm on the stars within 5kpc from the initial center until the shrinking sphere contains 50 particles. We take the outcome of the shrinking-sphere algorithm as \mathbf{r}_0 , and the CoM velocity of the stars in the 5kpc-sphere as \mathbf{v}_0 . The size of the sampling sphere, 1kpc and 5kpc for VELA and NIHAO, respectively, is chosen such that it is well above the spatial resolution of the simulation and is significantly smaller than R_{vir} (to avoid contaminations from massive satellite galaxies).

With visual inspections of the projected density maps of dark matter, gas, and stars, we find that the

centers defined above are sensible – although they are basically the locations of the highest stellar mass density, they overlap with the positions of the highest dark matter and gas mass densities within a couple of softening lengths, even during major mergers. We also verify that our main results are not sensitive to the definition of centers: using sampling spheres of $0.01R_{\text{vir}}$ or using the centers of dark matter instead of stars yields statistically indistinguishable results.

The spin parameters of cold⁵ gas (λ_{gas}) and stars (λ_{star}) are defined by eq. (1), with the sAM j measured within 10% of the virial radius R_{vir} . Dark matter halo spin is defined within R_{vir} . The AM J is defined about the origin ($\mathbf{r}_0, \mathbf{v}_0$). Throughout, we consider a *galaxy* to be the stars and cold gas within 10% of the virial radius of the host halo, and usually present the galaxy spin λ_{gal} measured from stars and cold gas combined, unless the spins of the stars and gas show different trends.

There is a corresponding dark-matter-only (DMO) simulation for each NIHAO galaxy. The DMO simulations adopt the same initial conditions as the hydro ones, and replace the gas particles with dark matter particles of the same mass. We measure the dark matter properties of the simulations with baryons, and mention the check on the DMO outputs when necessary.

⁵ Density $n_{\text{H}} > 1 \text{ cm}^{-3}$ and temperature $T < 10^4 \text{ K}$.

3 DISTRIBUTION OF SPIN FOR DIFFERENT COMPONENTS

Fig. 1 shows the cumulative distributions of the spins of the cold gas, stars and dark matter halo, for all snapshots after $z = 7$. The spin parameters of the different components are all well-described by log-normal distributions. Halo spin obeys a log-normal distribution with a mean of $\langle \lambda_{\text{halo}} \rangle = 0.037$, and a standard deviation of $\sigma_{\log \lambda} \simeq 0.2\text{-}0.25$, very similar to those found in N -body simulations (e.g. Bullock et al. 2001, Bett et al. 2007; Muñoz-Cuartas et al. 2011; Somerville et al. 2018; Lee et al. 2017a).

In both simulations, the stellar spin is ~ 5 times lower than the cold gas spin, which, in turn, is slightly lower than the halo spin. The cold gas spin is only 30-50% lower than halo spin, with $\langle \lambda_{\text{gas}} \rangle = 0.026$ (VELA) and 0.018 (NIHAO). This indicates that the radial specific angular momentum profile of the gas is higher than that of the dark matter, to the extent of $j_{\text{gas}}(0.1R_{\text{vir}})$ being comparable to $j_{\text{dm}}(R_{\text{vir}})$. Indeed, as discussed in Danovich et al. (2015), the gas streams have higher sAM than the dark matter streams at accretion to R_{vir} within a factor of two, but as they reach the inner halo, they are spinned down by the torque from the galactic disc. The scatter of λ_{gas} is somewhat larger than that of λ_{halo} , by $\sim 0.05\text{dex}$ in both cases.

The spin of cold gas (λ_{gas}) and of stars (λ_{star}) of the NIHAO simulations are systematically lower than those of VELA. There can be several possible reasons. First, as to the difference in gas spin, the gas properties are different between the two suites. Due to the relatively high density threshold of star formation, the gas in the NIHAO simulations can condense to higher densities than that in VELA before turning into stars. Due to the stronger stellar feedback, NIHAO galaxies have stronger exchange of AM between the cold galaxy range and the hot halo. Second, wet compaction, a process that high- z , stream-fed galaxies generally undergo, is efficient at raising λ_{gas} (see §6.1 for more details). The strength of compaction is expected to be sensitive to numerical resolution and feedback, so the NIHAO galaxies, of much coarser resolution and stronger feedback than VELA, generally show much weaker compactions. Finally, artificial losses of AM can occur in SPH simulations with limited resolution (Kaufmann et al. 2006). With a force softening length of a few hundred parsecs, and gas particle mass of a few times $10^5 M_{\odot}$, the NIHAO simulations could carry non-negligible numerical AM loss.

4 SPINS OF GALAXY VERSUS HALO

In this section, we characterize the correlation of the *amplitudes* of the spins of the galaxies and their host haloes, as well as the alignment of the spin *vectors*.

4.1 Spin amplitude

Fig. 2 presents galaxy spin versus host halo spin for all the galaxies at all snapshots at $z < 7$. Here, we

have tried to remove potential trends with halo mass or redshift as follows. First, the sample is binned into three redshift ranges, $z = 0\text{-}0.8$, $0.8\text{-}2$, and $2\text{-}7$, and two halo mass ranges, $M_{\text{vir}} > 10^{11.4} M_{\odot}$, and $< 10^{11.4} M_{\odot}$. We then calculate the median λ_{gal} and λ_{halo} for each mass and redshift bin, and for the whole sample. Finally, in the $\lambda_{\text{gal}}\text{-}\lambda_{\text{halo}}$ plane, the data points of different bins are shifted by the offset between the median point of the corresponding bin and that of the whole sample. As can be seen, there is almost no correlation between λ_{gal} and λ_{halo} in either NIHAO or VELA.

In fact, as shown in Fig. 3, there is negligible correlation in almost every (M_{vir}, z) bin at $z \gtrsim 0.8$ – the Pearson correlation coefficient \mathcal{R} seldom exceeds 0.3. There seems to be a correlation emerging in the lowest redshift bin in the NIHAO simulations, but it is still weak with $\mathcal{R} = 0.48$.

Danovich et al. (2015) showed that the sAM of gas and dark matter are strongly correlated at virial crossing,⁶ therefore, the lack of correlation between λ_{gal} and λ_{halo} means that the spin of baryons evolves differently with respect to that of the dark matter, inside the virial radius. That is, the angular momentum retention ratio, $f_j \equiv \lambda_{\text{gal}}/\lambda_{\text{halo}}$, must deviate from a constant of order unity, and vary from one galaxy to another and from time to time. We expect f_j to depend systematically on λ_{halo} – any mechanism that causes an anti-correlation between f_j and λ_{halo} can most efficiently erase the initial correlation between the sAM of baryons and dark matter in the cosmic web. Assuming for simplicity that the anti-correlation is parametrized by $f_j \propto \lambda_{\text{halo}}^b$ with a negative b , one can write

$$\log \lambda_{\text{gal}} = a + (1 + b) \log \lambda_{\text{halo}}, \quad (4)$$

where a is the zero point of the relation, and $(1 + b)$ is also a measure of the correlation strength between λ_{gal} and λ_{halo} (in addition to the Pearson \mathcal{R}), that ranges from proportionality ($1 + b = 1$) to no correlation ($1 + b = 0$).

The dashed lines in Fig. 3 are linear regressions of the form of eq. (4). Clearly, there is always $-1 \lesssim b < 0$ across all the redshift and halo mass bins. Hence, to smear out an initial correlation between the sAM of baryons and dark matter in the cosmic web, some mechanisms operate inside the halo such that initially high- λ_{halo} systems end up having lower- λ_{gal} ; and perhaps also that initially low- λ_{halo} systems end up with higher λ_{gal} . We discuss two possible mechanisms of this sort, wet compaction and mergers, in §6.

The left-hand panels of Fig. 3 show that, in the VELA simulations, λ_{gal} is higher in more massive haloes. As will be discussed in more detail in §6.1, this is basically a manifestation of galaxy compaction – galaxies above the mass threshold $M_{\text{vir}} \sim 10^{11.4} M_{\odot}$ are typically post compaction, where the sAM is higher due to

⁶ In fact, Danovich et al. (2015) found $\lambda_{\text{gas}} \simeq 1.5\lambda_{\text{dm}}$, with both λ_{gas} and λ_{dm} measured at $\gtrsim R_{\text{vir}}$. Gas spin at accretion is slightly higher, due to the higher quadrupole moment resulting from the early dissipative contraction of gas into the central cords of the thick dark matter filaments.

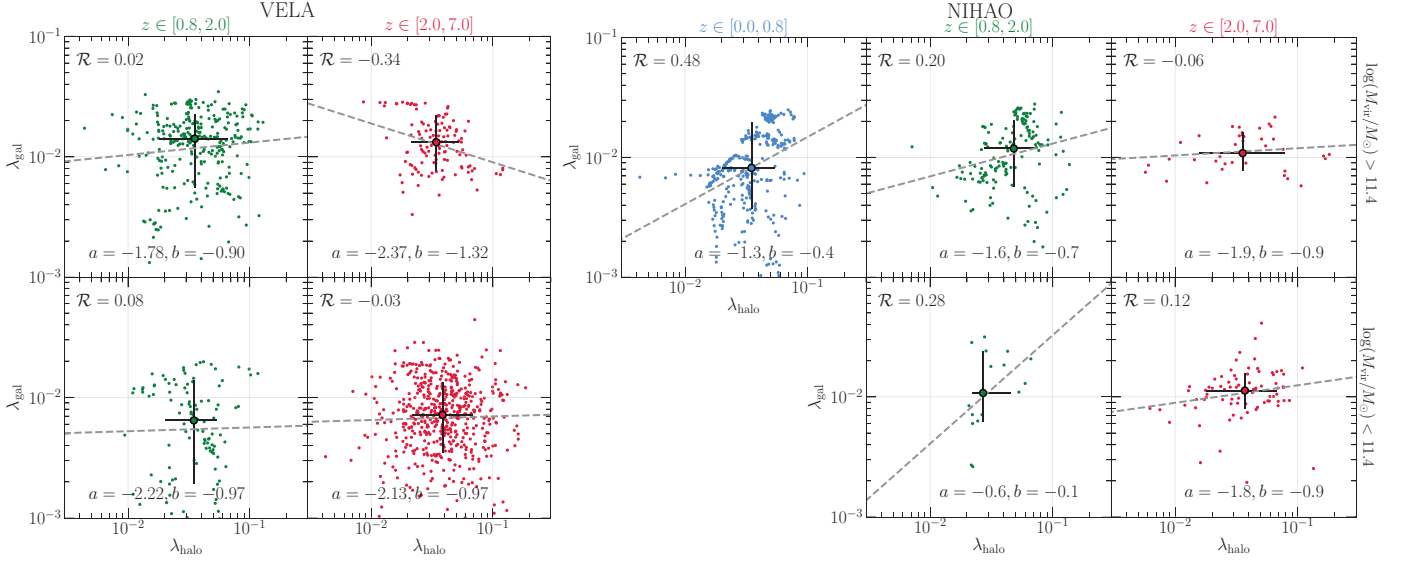


Figure 3. The spin of a galaxy (stars+gas within $0.1R_{\text{vir}}$) versus the spin of its host halo (DM within R_{vir}), in different bins of halo mass (upper: $M_{\text{vir}} > 10^{11.4} M_{\odot}$, lower: $M_{\text{vir}} < 10^{11.4} M_{\odot}$) and redshift, in the VELA simulation (left) and in the NIHAO simulation (right). Each dot is a galaxy at one snapshot. The big circles mark the medians with error bars indicating the 16th and 84th percentiles. The Pearson correlation coefficient \mathcal{R} is quoted at the upper left corner. The solid lines are linear regression of the form $\log \lambda_{\text{gal}} = a + (1+b) \log \lambda_{\text{halo}}$, with the best-fit parameters indicated. The VELA simulation exhibits negligible correlation throughout all the M_{vir} and z bins. λ_{gal} is higher by a factor of ~ 2 in systems with $M_{\text{vir}} > 10^{11.4} M_{\odot}$ or equivalently post compaction (see text in §6.1). In the NIHAO simulation, a weak correlation emerges at $z \lesssim 1$.

an extended ring that has formed from newly accreted gas.

By inspecting the spin of stars and cold gas separately, we verify that the results are qualitatively the same, with a weak to null correlation between either baryonic component within $0.1R_{\text{vir}}$ and the dark matter halo within R_{vir} .

4.2 Alignment

Although the amplitudes of spin are barely correlated, are the spin vectors of baryons and dark matter randomly oriented? To answer this question, we plot in Fig. 4 the cumulative distributions of $\cos \theta_{\text{gal,halo}} = \mathbf{j}_{\text{gal}} \cdot \mathbf{j}_{\text{halo}} / |\mathbf{j}_{\text{gal}}| |\mathbf{j}_{\text{halo}}|$ for different halo mass and redshift bins.

Generally, the median $\cos \theta_{\text{gal,halo}}$ is in the range of 0.6-0.7. Approximately 40% (20–30%) systems have $\cos \theta_{\text{gal,halo}} > 0.71$ (0.87), corresponding to an angle of $\theta_{\text{gal,halo}} < 45^\circ$ (30°). At a given halo mass, the alignment becomes marginally weaker at later times.

Comparing the two simulation suites, for the more massive haloes, NIHAO exhibits a slightly better alignment, with the median $\cos \theta_{\text{gal,halo}} = 0.65$ -0.72, while VELA shows a median of $\cos \theta_{\text{gal,halo}} = 0.50$ -0.62 depending on redshift. For the less massive cases, there seems to be a significant fraction with $\cos \theta \lesssim 0$. We note though, that the NIHAO results at $M_{\text{vir}} < 10^{11.4} M_{\odot}$ suffer from small-number statistics, and therefore opt not to overinterpret them.

Not shown here, we find the alignment between cold gas and halo to be better than that between

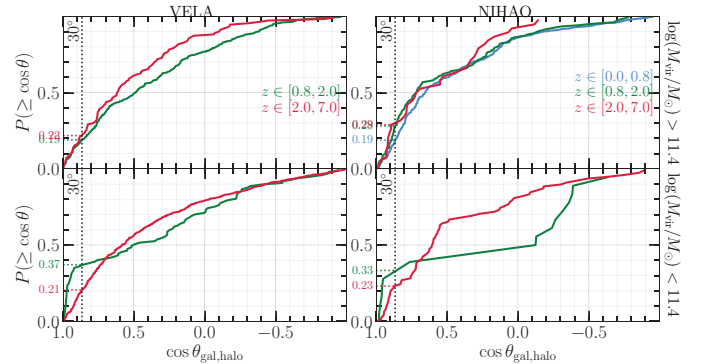


Figure 4. Cumulative distribution of the cosine of the angle between the angular momentum vectors of the galaxy (stars + cold gas within $0.1R_{\text{vir}}$) and that of the host halo (dark matter within R_{vir}), for VELA (left) and NIHAO (right) galaxies in different redshift and halo mass bins. Dotted lines mark the fraction of systems with $\theta < 30^\circ$. In VELA, the median $\cos \theta = 0.53$ -0.67, and seems to decrease (i.e., the alignment becomes marginally worse) at lower redshift. The NIHAO galaxies exhibit better alignment than VELA, with a similar, weak redshift trend. The lower- M_{vir} bin of NIHAO likely suffers from small-number statistics.

stars and halo. In particular, the NIHAO galaxies with $M_{\text{vir}} > 10^{11.4} M_{\odot}$ have a median $\cos \theta_{\text{gas,halo}}$ of 0.71-0.73 and a median $\cos \theta_{\text{stars,halo}}$ of 0.64-0.69 (depending on redshift weakly), compared to the corresponding VELA results of 0.59-0.68 and 0.48-0.62, respectively. For VELA galaxies with $M_{\text{vir}} < 10^{11.4} M_{\odot}$, the medians of $\cos \theta_{\text{gas,halo}}$ and $\theta_{\text{stars,halo}}$ are 0.57-0.63 and 0.53-0.57, respectively.

It is intriguing that the amplitudes of spins are

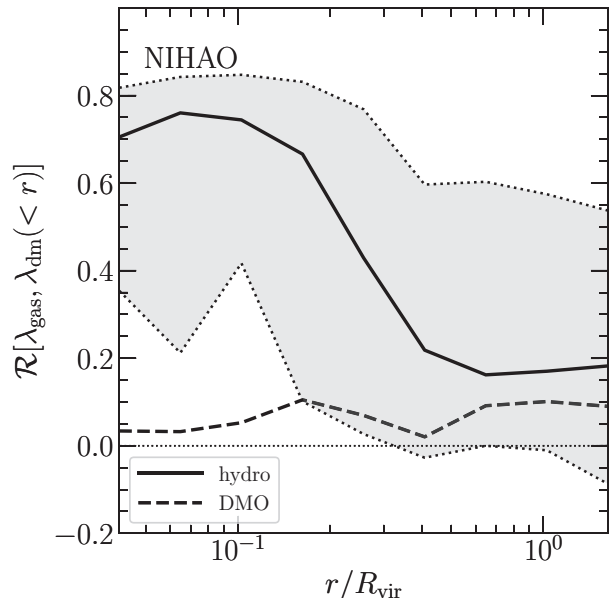


Figure 5. Correlation between the spin of cold gas measured within $0.1R_{\text{vir}}$ and the spin of dark matter within radius r , as a function of radius r , for the NIHAO galaxies. The *solid* line represents the median result over the redshift range $z = 0-7$. The dark matter spin is measured in the (fiducial) hydrodynamical simulation, with the shaded region bracketed by the dotted lines representing the 16th and 84th percentiles. The *dashed* line represents the median result, for which the dark matter spin is measured in the dark-matter-only (DMO) simulation that is complementary to the NIHAO simulation and that uses the same initial condition and replaces the gas particles in the fiducial NIHAO simulation with dark matter particles of equal mass. Gas spin is strongly correlated with the spin of dark matter out to $\sim 0.2R_{\text{vir}}$ if the dark matter spin is measured in the hydrodynamical simulation; while there is negligible correlation between gas spin and the dark matter spin measured in the DMO simulation.

uncorrelated although the alignment of the spin vectors is relatively good. It may well be that because the gas streams and the stellar disc are generally coplanar (Danovich et al. 2012), the torques that cause angular momentum gain or loss do not randomize the directions of the spin vectors.

4.3 Spin of galaxy versus inner halo

The correlation between the galaxy spin and the *whole* halo spin is weak, but the two parameters sample very different spatial scales. It may well be that the spin of the dark matter in the inner part of the halo, where the galaxy dwells, correlates with the galaxy spin better. To check this, we focus on the NIHAO galaxies, and measure the Pearson correlation coefficient between the gas spin, λ_{gas} , and the spin of the dark matter within radius r , $\lambda_{\text{dm}}(<r)$, at each snapshot, looking for a radius within which the dark matter spin is a good proxy of the gas spin.

The result is shown in Fig. 5. On average, there is a strong correlation ($\mathcal{R} \sim 0.7$) out to $r \sim 0.2R_{\text{vir}}$. Beyond $0.2R_{\text{vir}}$, the correlation drops quickly to negligible. The scatter of the correlation profile largely reflects redshift

dependence: the correlation is stronger at lower redshift, as already hinted in the right-hand panels of Fig. 3.

From the point of view of semi-analytic modelling, we are more interested to know whether or not one can use halo properties measured in N -body simulations to predict galaxy properties. Therefore, to test if $\lambda_{\text{dm}}(<0.2R_{\text{vir}})$ is an adequate galaxy spin indicator, we repeat the exercise, re-measuring $\lambda_{\text{dm}}(r)$ in the dark-matter-only (DMO) simulation complementary to the NIHAO sample. The DMO simulations adopt the same initial conditions as the fiducial NIHAO sample, and replace the gas particles with dark matter particles of the same mass. As shown by the dashed line in Fig. 5, the $\lambda_{\text{dm}}(<r)$ measured in the DMO simulation barely correlates with the gas spin, irrespective of radius r . Hence, the DMO inner halo spin, $\lambda_{\text{dm}}(<0.2R_{\text{vir}})$, is not eligible to be a proxy of galaxy spin as would be used in semi-analytic modeling, and baryonic processes influence the inner halo spin and cause an correlation. What specific mechanisms cause this correlation is beyond the scope of this study. Speculatively, the same processes could simultaneously be related to the null correlation between the galaxy spin and the whole halo spin.

5 SPINS OF GAS VERSUS STARS

Here we measure the correlation between the spins of stars and cold gas in the galaxy. On one hand, a correlation is expected to reflect the fact that stars have formed from cold gas and that the accreted stars and gas might have suffered similar torques. On the other hand, the stars may reflect the spin of the gas at earlier times, which may be different from that of the newly accreted gas.

5.1 Spin amplitude

As shown in Fig. 6, for the two simulation suites, the spins of the baryonic components are correlated, with $\mathcal{R} \sim 0.6-0.8$. In terms of redshift trend, both simulations seem to show a mildly stronger correlation at lower redshift. As for halo mass dependence, in the VELA sample, both λ_{gas} and λ_{star} are higher by $\sim 50\%$ for systems with $M_{\text{vir}} > 10^{11.4}M_{\odot}$ than for $M_{\text{vir}} < 10^{11.4}M_{\odot}$. NIHAO shows the same qualitative trend, although the baryonic spins in NIHAO are overall slightly lower than in VELA. NIHAO again exhibits marginally stronger correlations than VELA in general.

5.2 Alignment

Fig. 7 shows the cumulative distributions of $\cos\theta_{\text{gas,star}} = \mathbf{j}_{\text{gas}} \cdot \mathbf{j}_{\text{star}} / |\mathbf{j}_{\text{gas}}||\mathbf{j}_{\text{star}}|$. The gas and stellar spin vectors are generally well aligned. The median $\cos\theta_{\text{gas,star}}$ is 0.96-0.98 (0.96-0.99) in the VELA (NIHAO) simulation at $M_{\text{vir}} > 10^{11.4}M_{\odot}$, and is 0.88-0.92 in the VELA simulation at $M_{\text{vir}} < 10^{11.4}M_{\odot}$. The gas and stellar spin vectors are better aligned in more massive systems, and there seems to be a weak

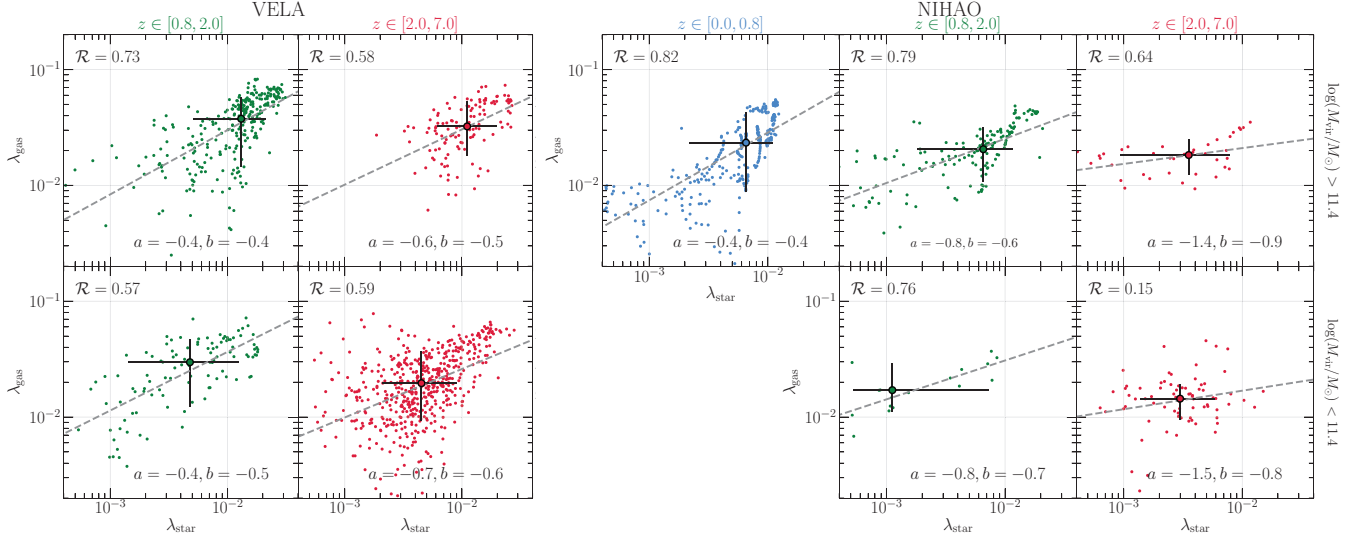


Figure 6. The spin of cold gas versus the spin of stars, for VELA (*left*) and NIHAO (*right*) galaxies in different bins of halo mass and redshift. In both VELA and NIHAO, the spins of the baryonic components are strongly correlated, and the correlation is stronger at later times. On average, the spin of either baryonic component is higher in more massive (post compaction) systems.

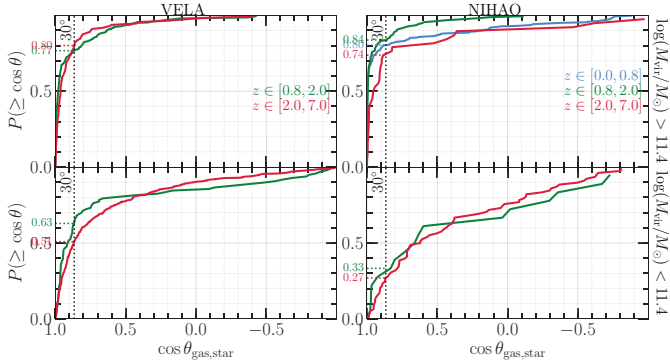


Figure 7. Cumulative distribution of the cosine of the angle between the angular momentum vectors of cold gas and stars, both measured within $0.1R_{\text{vir}}$, for VELA (*left*) and NIHAO (*right*) galaxies in different redshift and halo mass bins. The redshift and halo mass bins are the same as used in previous shows, as indicated. Dotted lines indicate the fraction of systems with $\theta < 30^\circ$. In both simulation suites, the spin vectors of the baryonic components are well aligned. The alignment is better in more massive systems, and strengthens marginally at later times.

trend that the alignment becomes marginally better at later times.

We notice that a non-negligible fraction of galaxies have *counter-rotating* gas and stellar components, especially the less massive ones. In particular, the fraction of having $\theta_{\text{gas,stars}} > 120^\circ$ is 5% (9%) and 0% (3%) in the VELA (NIHAO) simulation, for $M_{\text{vir}} < 10^{11.4} M_\odot$ and $> 10^{11.4} M_\odot$, respectively.

6 ORIGIN OF THE NULL CORRELATION BETWEEN GALAXY AND HALO SPINS

In this section, we discuss two mechanisms that can cause f_j to anti-correlate with λ_{halo} , and speculate on

other possible processes that can decouple λ_{gal} from λ_{halo} .

6.1 Effect of compaction

One possible origin for the anti-correlation between f_j and λ_{halo} is the dramatic compaction event that most galaxies undergo. Dekel & Burkert (2014) argued analytically, and Zolotov et al. (2015) and Tacchella et al. (2016) showed using simulations, that most galaxies undergo phases of dissipative gas contraction triggered by mergers or counter-rotating accretion streams, into compact, star-forming systems, termed “blue nuggets” (BN). These objects have been observed (Barro et al. 2013, 2014a,b, 2015b,a, 2016). Observationally, these compact star forming nuclei may be obscured by dust and are not necessarily blue in color. In the VELA simulations, compaction triggers inside-out quenching once above a threshold mass – stellar mass $10^{9.5-10} M_\odot$ and halo mass $10^{11-11.5} M_\odot$.

Wet compaction tends to occur when the incoming material has low sAM (Dekel & Burkert 2014). During the subsequent blue-nugget phase, the central gas is depleted to star formation and the associated outflows. These outflows preferentially eject low-AM gas, while the new incoming gas with higher spin settles in an extended ring (e.g. Fig. 7 in Zolotov et al. 2015). As a result, the gas spin in the galaxy is sharply rising during the BN phase. This implies that with a low λ_{gas} at halo entry (presumably reflecting low λ_{halo} , Danovich et al. 2015), the galaxy, that undergoes compaction, ends up having a higher λ_{gas} , namely $\lambda_{\text{gal}}/\lambda_{\text{halo}} > 1$.

The spin of stars exhibits a similar behavior. During the BN phase, new stars form in the center following the compact gas, but after the BN phase the stellar effective radius is gradually growing, partly due to new stars that form in the outer ring with high AM and partly due to

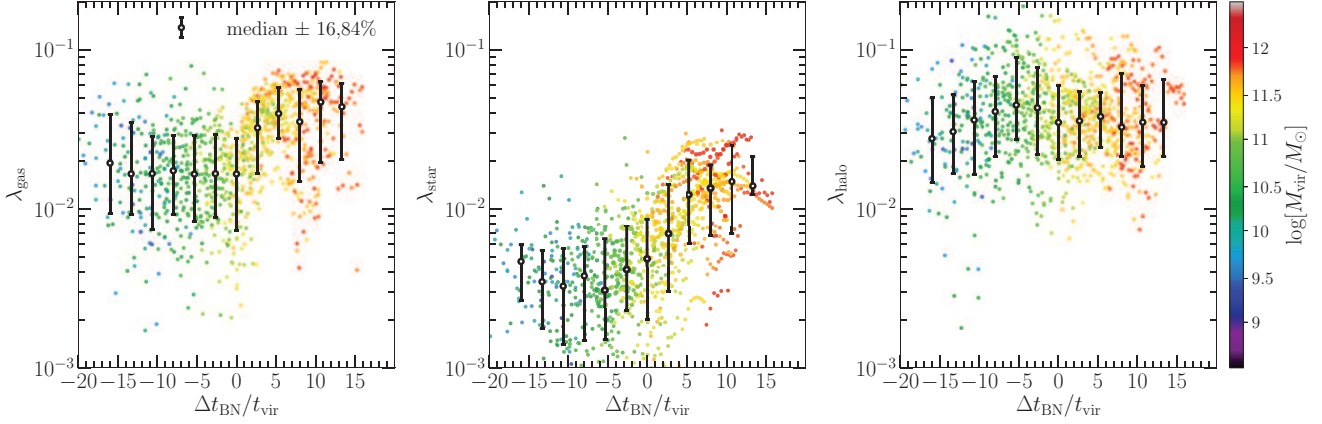


Figure 8. The spin of cold gas, stars (within $0.1R_{\text{vir}}$), and dark matter halo (within R_{vir}) versus $\Delta t_{\text{BN}}/t_{\text{vir}}$ in the VELA simulation, where $\Delta t_{\text{BN}}/t_{\text{vir}}$ is the time to the BN snapshot in units of virial time. The spins of baryons are rising after the compaction event, due to the formation of an extended ring, while λ_{halo} remains roughly constant. Color marks halo mass, indicating that compactions in VELA generally occurs at $\gtrsim 10^{11-11.5}M_{\odot}$.

new ex-situ stars from minor mergers, likely with higher AM.

We illustrate this effect using the VELA simulations. We detect the main BN phase by identifying the snapshot of the most prominent increase in the surface gas density within 1kpc (see Dekel et al. 2018, in prep., for more details), and investigate the evolution of the spins of different components before and after the main BN phase. Fig. 8 shows λ_{gas} , λ_{star} and λ_{halo} versus $\Delta t_{\text{BN}}/t_{\text{vir}}$, the time from the BN phase in units of virial time. Clearly, compaction affects the spins of baryons as aforementioned, but not the spin of the dark halo. Since compactions are more common at high- z , this, combined with the correlation of compaction and low λ_{halo} reported in Zolotov et al., explains the anti-correlation between f_j and λ_{halo} at high z . Compaction also generally occurs at $M_{\text{vir}} \simeq 10^{11-11.5}M_{\odot}$, explaining the higher λ_{gal} in more massive haloes as we have seen in the left-hand panels of Fig. 2. We caution though that the post-compaction ring formation is hypothetical. The suppression of star formation by AGN feedback may become important for post-compaction systems and turn BNs into compact quiescent systems (“red suggests”) quickly. Without AGNs, the VELA simulations may over-estimate the significance of the post-compaction ring phase.

6.2 Effect of mergers

Another possible source for the anti-correlation of f_j and λ_{halo} is the variations of spin during a major merger.⁷ The accretion of a large satellite makes λ_{halo} rise, as the spin is temporarily dominated by the orbital angular momentum of the merging dark matter haloes. The galaxy spin λ_{gal} is temporarily unaffected unless the satellite survives the tidal disruption and reaches

⁷ Since the compaction is in many cases associated with a merger, the two may affect f_j simultaneously.

the central baryonic range. In such case, within a couple of halo dynamical times, λ_{halo} relaxes to its normal value as some of the high AM material ends up beyond R_{vir} (Lee et al. 2017b), but λ_{gal} rises, as the orbital angular momentum of the baryonic components now dominates the galaxy spin. This two-phase process is expected to introduce an anti-correlation between f_j and λ_{halo} .

We illustrate this effect using the NIHAO simulations. We detect halo mergers as mass increments of the main progenitor more than 10% (i.e., major and minor mergers).⁸ If there are multiple detections of mergers within two halo dynamical times, $t_{\text{vir}} \equiv R_{\text{vir}}/V_{\text{vir}}$, we only keep the earliest one, to avoid double counting the re-accretion of splashback satellites. This gives us a clean, but not necessarily complete sample of massive mergers. Fig. 9 shows the spin ratio f_j , with respect to that at the moment of a halo merger $f_j(0)$, as a function of the time after halo merger, $\Delta t_{\text{HM}}/t_{\text{vir}}$. Clearly, f_j drops abruptly upon the accretion of a large satellite, and starts to recover after $\sim 2t_{\text{vir}}$. We verify that VELA simulations also show the decrease-and-recover behavior of f_j . As with compaction, massive mergers are also more frequent at high- z , helping to partly explain the anti-correlation between f_j and λ_{halo} at high z . We caution that both effects are more common at higher masses, and the low mass bin perhaps requires other explanations.

6.3 Other reasons for the lack of correlation

While the two mechanisms discussed above generate some anti-correlation, we learn that they are not enough

⁸ A mass ratio of 1:10 between the satellite and the central is chosen such that 1) orbit decay due to dynamical friction is efficient; 2) the time interval between two mergers is long enough to allow for the characteristic evolution pattern of spins as described above.

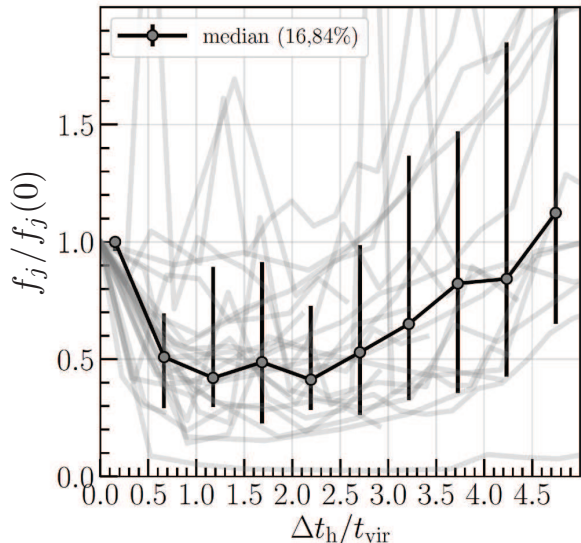


Figure 9. The ratio $f_j \equiv \lambda_{\text{gal}}/\lambda_{\text{halo}}$ with respect to f_j at the moment of a massive halo merger (see text) as a function of the time after the merger, $\Delta t_{\text{HM}}/t_{\text{vir}}$, for the NIHAO galaxies. Thin grey lines are individual cases; the thick line with error bars indicate the median and 16 and 84 percentiles. f_j decrease immediately after halo merger and start to recover after ~ 2 virial times, both phases giving rise to an anti-correlation between f_j and λ_{halo} .

for explaining the full effect. For example, removing the post-halo-merger snapshots within $4t_{\text{vir}}$ in the VELA simulation results in a positive, but rather weak correlation between λ_{gal} and λ_{halo} , with $\mathcal{R} \approx 0.3$. The two mechanisms are tightly related – in fact, about 40% of compactations are preluded by massive mergers, and the rest are associated with minor mergers, disk instabilities, counter-rotating streams, or other mechanisms (Dekel et al. 2018, in preparation). Here we speculate on a few other possible processes that may smear out the $\lambda_{\text{gal}}-\lambda_{\text{halo}}$ correlation but do not necessarily cause an anti-correlation between f_j and λ_{halo} . We refer interested readers to Danovich et al. (2015), for a comprehensive discussion of different stages of AM build up for galaxies at high- z .

First, λ_{gal} and λ_{halo} are quantities reflecting different time domains. The spin of gas reflects the sAM of recently accreted cold gas, while the spin of the dark matter halo is an integration of the full assembly history. Therefore variations in the incoming streams from the cosmic web affect λ_{gas} more and λ_{halo} less. This is in line with our finding that λ_{gal} and λ_{halo} are particularly uncorrelated at high z , when both gas accretion and depletion (star formation) are much faster.

Second, gas ejection from the galaxy center due to stellar feedback tends to remove low-spin gas, mixes the gas in the hot halo, and recycles the gas if it cools (e.g., DeFelippis et al. 2017). Gas outflows can also occur from the disk outskirts, which removes high-spin gas that returns with low spin, thus lowering the overall spin (DeGraf et al. in prep.). Hence, stronger feedback generally means more AM exchange between the inner and outer halo. However, stronger feedback also means less clumpiness, so the processes that facilitate

AM transfer such as dynamical friction, ram pressure, and torques generated by the perturbed disk under violent disk instability (Dekel, Sari & Ceverino 2009) may be less efficient. We note that the NIHAO simulations, which have stronger stellar feedback than VELA, show better alignment between spin vectors, and marginally stronger $\lambda_{\text{gal}}-\lambda_{\text{halo}}$ correlation. Therefore, it seems that the net effect of a strong feedback is working for a better correlation or alignment. However, this interpretation is hindered by the fact that NIHAO has poorer resolution, which also reduces the clumpiness of the galaxies (Buck et al. 2017).

Third, torques from the stellar disk on the inspiraling gas ring can spin down the galaxy, not affecting λ_{halo} . Balancing this effect, compaction gives rise to a central bulge, and thus less torque on the inspiraling gas and less angular momentum loss.

To conclude, the evolution of λ_{gal} is the net effect of many coupled processes, and the null correlation between λ_{gal} and λ_{halo} is not very surprising.

7 GALAXY SIZE PREDICTOR REVISITED

What we have learnt so far poses a challenge to the classic galaxy-size predictor

$$R_e \simeq f_j \lambda_{\text{halo}} R_{\text{vir}}. \quad (5)$$

We showed that the proportionality factor f_j ($\equiv \lambda_{\text{gal}}/\lambda_{\text{halo}}$) has very large scatter, and can vary on short time scales due to compaction, mergers, and other processes. The factor f_j depends systematically on λ_{halo} : when parametrized as $f_j \propto \lambda_{\text{halo}}^{-b}$, the simulations show that $b \approx -1$ at high z , suggesting that λ_{halo} is not a good predictor of galaxy size, at least at $z \gtrsim 1$.

Here we check the validity of eq. (5) with the VELA and NIHAO simulations. The left-hand panels of Figs. 10 - 11 show R_e/R_{vir} versus λ_{halo} for the VELA and NIHAO galaxies across all snapshots at $z < 7$. Note that in Fig. 11 and for the rest of the paper, we have included the full NIHAO sample of ~ 100 galaxies whose M_{vir} range from $10^{9.5} M_{\odot}$ to $10^{12.5} M_{\odot}$. The full sample, with respect to the MW-sized subsample, shows the same trends regarding R_e versus R_{vir} , and helps with the statistics.

There is almost no correlation between R_e/R_{vir} and λ_{halo} , independent of redshift. Interestingly, the right-hand panels of Figs. 10 - 11 show that both simulation suites still nicely reproduce the observed relation $R_e \approx AR_{\text{vir}}$, with the overall best-fit $A \approx 0.024$. In addition, both suites show a clear redshift trend: the proportionality factor A increases from $\simeq 0.02$ at $z \lesssim 1$ to 0.03-0.04 at $z \sim 3$, and to approximately 0.05 at $z \gtrsim 5$. This redshift trend qualitatively agrees with what Somerville et al. (2018) found using the GAMA and CANDELS surveys and abundance matching, but is a bit too strong.

That is, in the simulations, the relation $R_e \approx AR_{\text{vir}}$ naturally arises, although A is not a function of λ_{halo} . The interesting questions become: *what determines the*

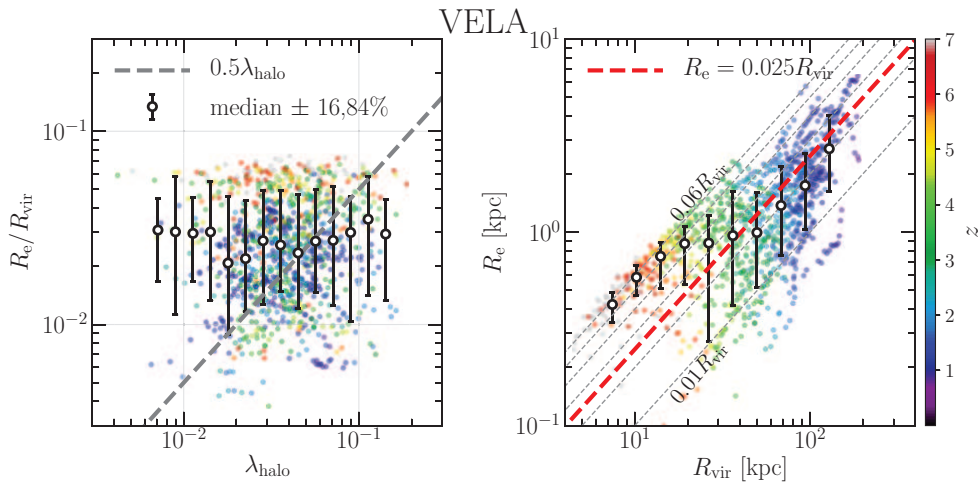


Figure 10. Galaxy size (3D half-stellar mass radius) to host halo virial radius ratio versus halo spin (*left*), and galaxy size versus host halo virial radius (*Right*), colorcoded by redshift, in the VELA simulations. Circles with errorbars indicate the median and 16 and 84 percentiles. Dashed line in the left-hand panel represents a reference line, $R_e = 0.5\lambda_{\text{halo}}R_{\text{vir}}$. Somerville et al. (2018) showed that this relation, when combined with the stellar to halo mass relation from abundance matching, reproduces the observed R_e - M_* relations across redshift up to $z \sim 3$. Dotted lines in the right-hand panel are loci of $R_e = AR_{\text{vir}}$, with $A = 0.01, 0.02, \dots, 0.06$. The overall best-fit A is 0.025 (red, dashed line), while obviously A increases with increasing redshift, in qualitative agreement with observation.

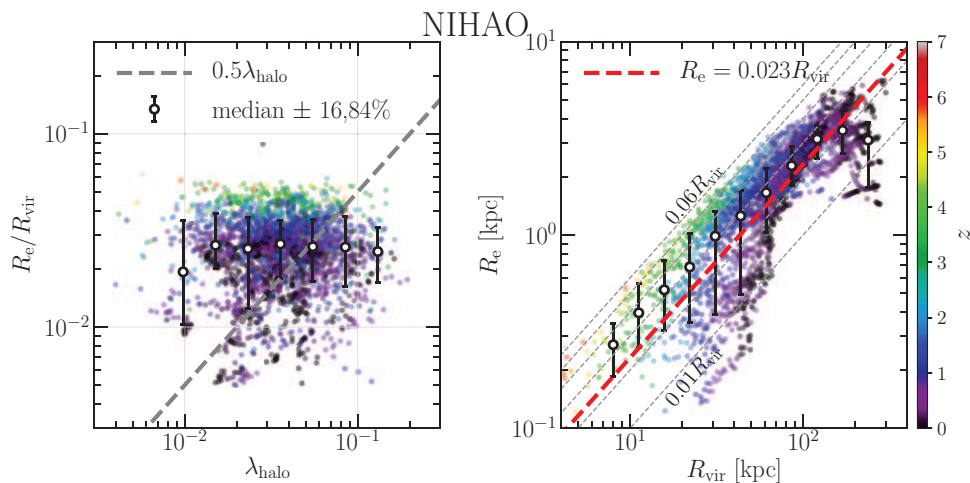


Figure 11. The same as Fig. 10, but for the NIHAO simulation. Overall, $R_e = AR_{\text{vir}}$ with $A = 0.023$, similar to that of VELA. The redshift dependence of A is in qualitative agreement with VELA.

value of A ? Are there any secondary halo properties (secondary to halo mass or R_{vir}) that can capture the scatter in A ? What gives rise to the redshift dependence? Our goal here is to generalize from the simulations an empirical recipe for predicting galaxy size using solely halo properties that can be useful for semi-analytic or semi-empirical models.

7.1 a new empirical galaxy size predictor

It turns out that, at fixed halo mass, smaller galaxies tend to live in more concentrated haloes, where the halo concentration parameter is defined as $c \equiv R_{\text{vir}}/r_s$, with r_s the scale radius of the best-fit Navarro, Frenk & White (1997) profile. We measure the

concentration parameter by fitting an NFW circular velocity profile to the circular velocity profile $V_c(r)$ of the dark matter component of the simulated galaxy, as detailed in Appendix A. Assuming for simplicity a power-law dependence on c , we find that galaxy size scales with halo radius and concentration as

$$R_e = A' c^\gamma R_{\text{vir}}, \quad (6)$$

with $\gamma \approx -0.7$ in both simulation suites. As such, eq. (6) is a tighter relation than $R_e = AR_{\text{vir}}$, and the factor A' is almost independent of redshift or mass.

We note that the role of the concentration dependence is two-fold. First, at fixed halo mass and redshift, the size of *individual* galaxies anti-correlates with halo concentration. The anti-correlation is well approxi-

mated by $c^{-0.7}$. We illustrate this point in Appendix B. Second, there is a redshift dependence associated with $c^{-0.7}$, which captures the evolution of the average R_e -to- R_{vir} ratio. It is well established that halo concentration is a function of halo mass and redshift. Using N -body simulations of the Planck cosmology, Dutton & Macciò (2014) provide an empirical concentration-mass-redshift relation, given by

$$\log\langle c \rangle = a + b \log(M_{\text{vir}}/10^{12}h^{-1}M_{\odot}) \quad (7)$$

where $a = 0.537 + 0.488 \exp(-0.718z^{1.08})$ and $b = -0.097 + 0.024z$. For $M_{\text{vir}} \sim 10^{12}M_{\odot}$, this relation is well approximated by $\langle c \rangle \propto (1+z)^{-0.75}$ up to $z \sim 3$. Therefore, with the factor $c^{-0.7}$, eq. (6) indicates that $A \propto (1+z)^{0.5}$, as found in both VELA and NIHAO. This is illustrated in more detail in Appendix C.

Fig. 12 and Fig. 13 show R_e versus R_{vir} in the left-hand panels, and R_e versus the concentration-corrected halo radius, $(c/10)^{-0.7}R_{\text{vir}}$, in the right-hand panels, for VELA and NIHAO respectively. Clearly the concentration scaling leads to a tighter and more universal relation for both suites.

From the perspective of semi-analytic models, which build upon DMO simulations, we also check the validity of eq. (6) using concentrations and virial radii measured from the matching DMO snapshots of the NIHAO simulations. This is shown in Fig. 14. Comparing Fig. 13 and Fig. 14, we can see that the same recipe holds, although the best-fit A' is somewhat different, reflecting the average halo response to baryonic physics. We conclude that galaxy half mass radius *in the simulations* can be empirically modeled as $A'(c/10)^{-0.7}R_{\text{vir}}$, with A' of the order of 0.02 and slightly dependent on the details of baryonic physics.

Intuitively, the dependence of galaxy size on halo concentration can be rationalized as follows. When considering a fixed halo mass, the concentration measures the depth of the gravitational potential well. For an NFW profile, $\Phi_0 = -V_{\text{vir}}^2 c/f(c)$, where Φ_0 is the gravitational potential at the center of the halo, V_{vir} is the virial velocity, and $f(x) = \ln(1+x) - x/(1+x)$. In this regard, the success of eq. (6) simply indicates that galaxy size contains information about the depth of the host potential, such that smaller galaxies live in deeper potential wells, possibly due to the fact that these haloes tend to form earlier (e.g., Wechsler et al. 2002; Zhao et al. 2009). While the above reasoning is suggestive, the cause of the concentration dependence of R_e/R_{vir} is posed here as a theoretical challenge, especially the origin of the slope $\gamma \simeq -0.7$ in eq. (6).

8 DISCUSSION

8.1 Comparison with previous studies

In this section, we compare our results regarding the correlations of spin amplitudes and spin vectors with those reported in the literature.

Teklu et al. (2015) use the Magneticum Pathfinder simulations to study the connection between the kinematic morphology of galaxies and their specific baryonic

AM and host halo spin. Although their primary focus is the morphology dependence, Fig.11 therein actually shows that the sAM of the halo j_{halo} and the sAM of the cold gas j_{gas} are barely correlated at $z > 1$, for either disks or spheroids. This is in agreement with what we find in VELA and NIHAO.

In addition, Teklu et al. (2015) show that at lower redshifts there is a weak correlation coming into place, consistent with what NIHAO implies. We have verified using the Illustris simulations (Genel et al. 2014) that at $z \gtrsim 1$ the spin of baryons and the spin of the host halo are barely correlated, and that at lower- z there is a weak correlation developing primarily between λ_{star} and λ_{halo} . The low- z behavior is also confirmed by Rodriguez-Gomez et al. (2017), who report a correlation in the Illustris simulation between the degree of rotation-support of stars and host halo spin for $z = 0$ galaxies with $M_{\star} < 10^{11}M_{\odot}$.

We note that both the Magneticum Pathfinder simulations and the Illustris simulations have taken AGNs into account, and exhibit similar results compared to VELA and NIHAO. Therefore, AGNs seem to have rather weak effect regarding the $\lambda_{\text{gal}}\text{-}\lambda_{\text{halo}}$ correlation.

We find the alignment of galaxy spin and halo spin to be marginally weaker at later times, and the alignment of gas spin and stellar spin to become slightly better at later times. The same qualitative trends are found by Zjupa & Springel (2017) in the Illustris simulation, where the spins of dark matter, gas and stars are all measured within the whole virial radius.

The median angle between the spin vectors of the cold gas and the host halo, $\langle \theta_{\text{gas,halo}} \rangle$, is 43-45° in the NIHAO simulations, weakly dependent on redshift. This is in good agreement with most of the reported values in the literature: Hahn, Teyssier & Carollo (2010) found 49° at $z = 0$; Teklu et al. (2015) found 45-49° at $z = 0.1$, depending weakly on galaxy morphology. Sharma, Steinmetz & Bland-Hawthorn (2012) reported a significantly smaller value of 30°. The median $\langle \theta_{\text{gas,halo}} \rangle$ is 47-54° for VELA galaxies with $M_{\text{vir}} > 10^{11.4}M_{\odot}$, and is 51-55° for $M_{\text{vir}} < 10^{11.4}M_{\odot}$, depending on redshift. These results are on the high side of the literature values.

The median angle between the spin vectors of the stars and the host halo $\langle \theta_{\text{stars,halo}} \rangle = 46\text{-}50^\circ$ in the NIHAO simulations, also in good agreement with previous studies. Croft et al. (2009) found 44° at $z = 1$; Hahn, Teyssier & Carollo (2010) measured 49° at $z = 0$; Teklu et al. (2015) found 46-57° at $z = 0.1$; Bett et al. (2009) reported a significantly smaller value of 34° at $z = 0$; in comparison, at $z < 0.8$, $\langle \theta_{\text{stars,halo}} \rangle = 49^\circ$ in NIHAO. VELA results are again on the high side, with $\langle \theta_{\text{stars,halo}} \rangle = 61^\circ$ at $z = 0.8 - 2$.

By tracing the Lagrangian volumes of the inner 10% of the virial radii at $z = 0$, Zavala et al. (2016) found that the angular momentum loss of baryons tightly correlates with that of the dark matter, since the turnaround time of the dark matter. This is in line with our finding that the spins of the inner halo and the galaxy are correlated.

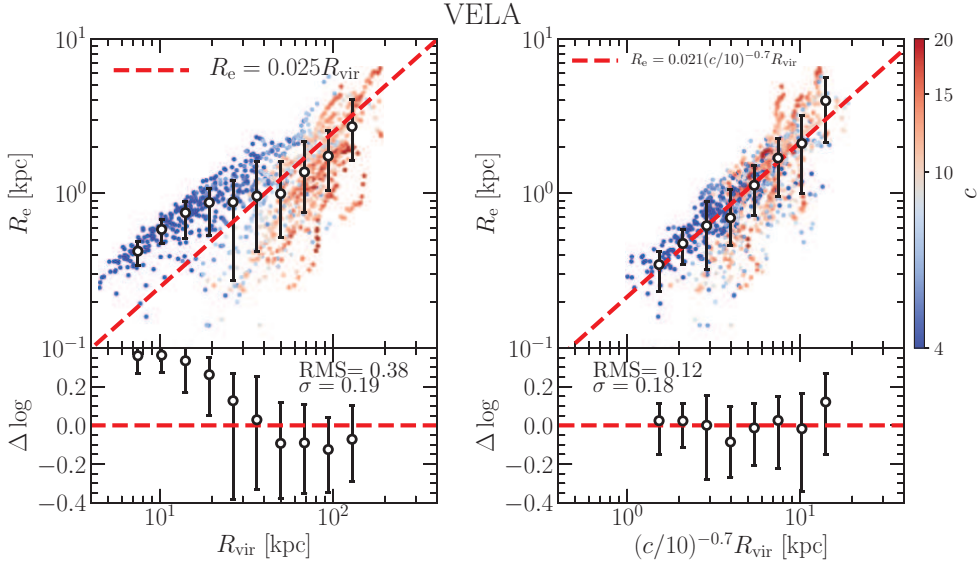


Figure 12. *Left:* galaxy size (3D half-stellar mass radius) R_e versus halo virial radius R_{vir} , for the VELA simulations throughout redshifts ($z = 0.8 - 7$), color-coded by halo concentration. The red, dashed line is the best-fit relation of the functional form of $R_e = AR_{\text{vir}}$, as indicated. *Right:* galaxy size R_e versus the concentration-corrected halo radius, $(c/10)^{-0.7} R_{\text{vir}}$. The red, dashed line is the best-fit relation of the form of $R_e = A'c^\gamma R_{\text{vir}}$, with $\gamma = -0.7$ fixed. Circles with error bars indicate the median and the 16th and 84th percentiles. The *bottom* panels show the residual with respect to the best-fit model. The quoted numbers are: the root-mean-square of the medians with respect to the best-fit models, and the average 1σ scatter of R_e in the bins of halo radius. The concentration scaling makes the relation between galaxy size and halo radius tighter and more universal.

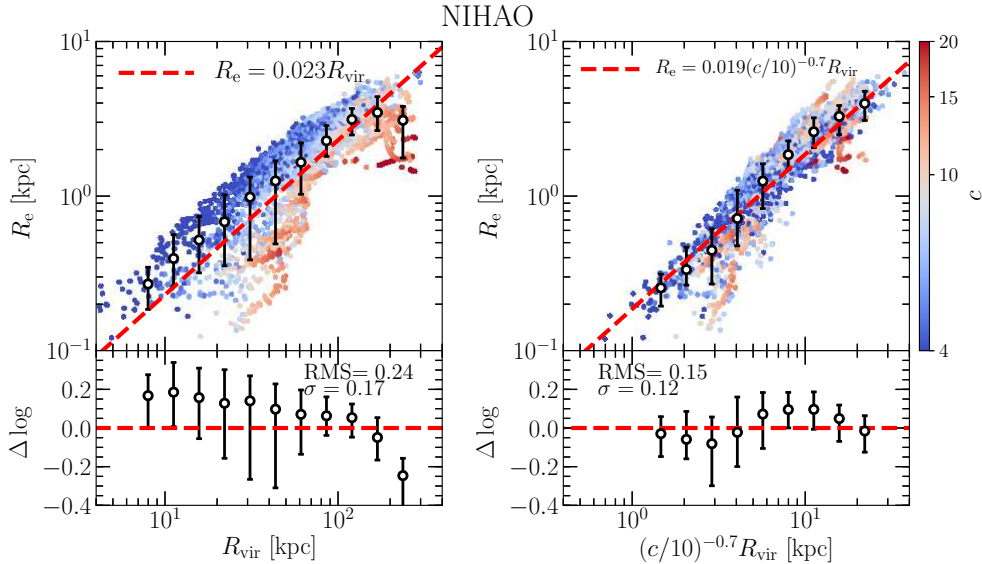


Figure 13. The same as Fig. 10, but for the NIHAO simulations ($z = 0 - 7$). The same concentration-scaling, $R_e \propto c^{-0.7} R_{\text{vir}}$, works equally well for NIHAO, with a similar zero-point as found in VELA.

Hahn, Teyssier & Carollo (2010) and Teklu et al. (2015) found the median angle between the spin vectors of the baryonic components to be $\langle \theta_{\text{gas,stars}} \rangle \approx 6 - 8^\circ$ for late-type galaxies, with very weak redshift dependence in the range $z = 0 - 2$. This is bracketed by the NIHAO result of 5° at $z < 2$ and the VELA result of 13° at $0.8 < z < 2$.

Starkenburger et al. (2018, in prep) study the counter-rotating galaxies in the Illustris simulation in detail. They find the counter-rotating fraction to be very low. The fraction of galaxies with the angle between the spin vectors of the gas and stars larger than 120° is 0.43%, independent of halo mass for $M_{\text{vir}} = 10^{11.4-12.2} M_\odot$ and decreasing at higher masses (private

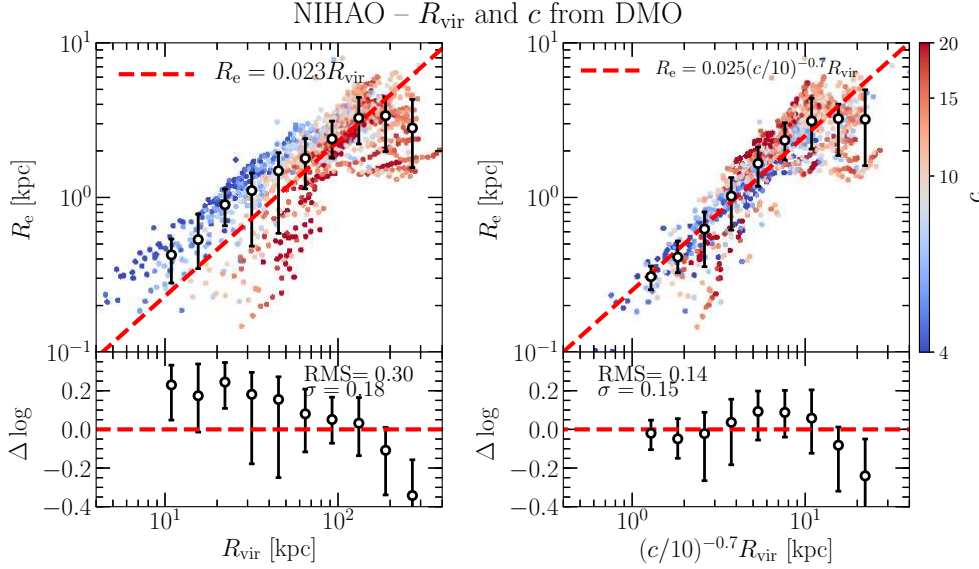


Figure 14. Similar to Fig. 13, but with the halo properties measured in the matching dark-matter-only simulations. The data points are sparser than in Fig. 13 because for every four hydro output snapshots there is only one dark-matter-only output. The same empirical relation $R_e \propto c^{-0.7} R_{vir}$ holds, although the scatter is somewhat larger. The difference between the zero point here (0.025) and in Fig. 13 (0.019) reflects the average halo response to baryonic processes in the NIHAO simulations.

communication). Note that the Illustris sample is generally more massive than the galaxies used in this study, so it is possible that counter-rotations are more common in low mass systems. In fact, for $M_{vir} > 10^{11.4} M_\odot$, no counter-rotation defined in the same way is detected in VELA, consistent with Starkenburg et al.

8.2 Redshift dependence of R_e in comparison with observations

We note that, while eq. (6) with $\gamma \simeq -0.7$ accurately describes the simulation results, the implied redshift dependence of R_e/R_{vir} seems too strong compared to that inferred from halo abundance matching (Somerville et al. 2018). In particular, the concentration scaling $c^{-0.7}$ yields approximately $R_e/R_{vir} \propto (1+z)^{0.5}$, while the observationally inferred redshift trend is approximately $\propto (1+z)^{0.3}$. This is illustrated in Appendix C.

The key observational benchmark for a galaxy size predictor is the R_e – M_* relation, which exhibits clear redshift evolution such that, at fixed M_* , galaxies are more compact at higher z (e.g., van der Wel et al. 2014; Somerville et al. 2018). In the context of empirical modeling of observations, the prediction of the R_e – M_* relation requires the combination of the relation between the stellar mass and halo mass from abundance matching and the relation between galaxy size and halo radius from theory. In practice, starting from the halo catalog of an N -body simulation, one converts M_{vir} to M_* using the M_* – M_{vir} relation, and computes R_e using R_{vir} and halo structural parameters (λ_{halo} , c) according to the size predictor.

As said, eq. (6) exhibits a z -dependence that is too

strong. At $z \sim 2$, the average galaxy size predicted by $R_e = 0.02(c/10)^{-0.7} R_{vir}$ is $\sim 50\%$ higher than the 3D-half mass radius observed in CANDELS deduced by Somerville et al. (2018).

We opt not to interpret this tension too literally, for two reasons. First, the half-mass radius as deduced from the observed 2D radius may be biased as a function of redshift, and second, the M_* – M_{vir} relation may carry non-negligible uncertainties, as follows.

The deprojection from 2D to 3D may be strongly biased. The conversion of the projected half-light radius ($R_{e,2D}$) to the 3D half-stellar-mass radius (R_e) involves two factors:

$$R_{e,2D} = f_p f_k R_e, \quad (8)$$

where f_p corrects for projection and f_k accounts for the conversion from light-weighting to mass-weighting. While f_k (~ 1.2) seems to be a weak function of mass and redshift (Dutton et al. 2010; Lange et al. 2015), f_p depends significantly on the structure and shape of galaxies and is very likely a strong function of redshift and mass. For spherically-symmetric spheroids or oblate systems, f_p is typically between 0.68 (de Vaucouleurs) and 1 (face on exponential disk), but for elongated (prolate) systems, f_p can easily be much smaller than unity. Qualitatively, this can be comprehended by considering a cigar-shaped galaxy projected along the major axis. It is easy to show that ellipsoids with an intrinsic axis ratio of $b/a \sim 0.4$, f_p has a value of ~ 0.5 for exponential density profiles. The fraction of prolate galaxies increases towards high redshifts and lower masses: at $z \sim 1$, more than half of all the galaxies with $M_* \sim 10^9 M_\odot$ are prolate (van der Wel et al. 2014, Zhang et al. in prep). This is supported by simulations. In fact, VELA galaxies typically have $b/a \sim 0.4$ at $z = 2$ –

2.5 (Ceverino, Primack & Dekel 2015; Tomassetti et al. 2016).

Somerville et al. (2018) practically applied $f_p f_k = 1 \times 1.2 = 1.2$ for late-type galaxies and $f_p f_k = 0.68 \times 1.15 = 0.78$ for early-type galaxies. That is, for the relevant mass range ($M_\star \lesssim 10^{10.5} M_\odot$) where late-type galaxies dominate, R_e is approximately always 20% smaller than $R_{e,2D}$, while for prolate systems, which dominate at high redshifts, it should be significantly larger than $R_{e,2D}$. Taking the effect of projecting elongated systems into account will increase the R_e deduced from observations and potentially alleviate the tension.

The M_\star - M_{vir} relations may carry non-negligible systematic uncertainties. Almost all the abundance matching studies assume a Chabrier (2003) initial mass function (IMF) as found for the Milky Way throughout redshifts. However, the IMF may not be universal. In fact, even in the local universe, there is no consensus whether the IMF is Milky-Way like or bottom heavy (e.g., Dutton, Mendel & Simard 2011). If the IMF is closer to Salpeter (1955) at $z \sim 2$, the stellar mass would be higher by ~ 0.25 dex with respect to the standard abundance matching result based on the Chabrier IMF. This alone almost adequately accounts for the 50% overprediction of the R_e - M_\star relation.

If the goal, despite these caveats, is to reproduce the observational estimates as they are, using the standard abundance matching result, one can simply introduce an extra redshift-dependence (in addition to and in the opposite direction to that associated with $c(z)^{-0.7}$) by generalizing eq. (6) to

$$R_e = A'(1+z)^\beta c^\gamma R_{\text{vir}}. \quad (9)$$

We find that $\beta \approx -0.2$ serves as an adequate correction for $\gamma = -0.7$.

We clarify again that eq. (9) is a deviation from eq. (6) that accurately describe the redshift dependence in the simulations. Eq. (9) should be adopted if the tension between the simulated sizes and the sizes deduced from observations at high redshift is confirmed to be valid.

8.3 Other comments

We also note that, although the concentration parameter has been used in conventional galaxy size predictors of the form of eq. (5), its role was rather limited. In recipes of the sort of Mo, Mao & White (1998), concentration comes in via a factor of order unity that describes the adiabatic contraction of the halo due to the gravity from the galactic disk. Here, with eq. (9) and $\gamma \approx -0.7$, the c -dependence is more pronounced.

The concentration dependence may also *partially* explain the morphology dependence of the R_e - R_{vir} relation. In the context of conditional abundance matching, the specific star formation rate (color) of a galaxy contains information of the host halo formation time, in the sense that older galaxies dwell in haloes that formed earlier at a given mass (Hearin & Watson 2013). Galaxy color correlates with morphology, and concentration reflects halo formation time. That is, eq. (9) hints that

quiescent galaxies are more compact at a given halo mass (virial radius) than star-forming ones.

The most prominent difference between VELA and NIHAO in Figs. 12 - 13 is that the scatter is larger in VELA for both the $R_e - R_{\text{vir}}$ relation and the $R_e - c^{-0.7} R_{\text{vir}}$ relation. This is likely because the NIHAO sample consists of almost exclusively large, late-type galaxies, while the VELA suite covers a wider range of morphologies. The fact that the $R_e - c^{-0.7} R_{\text{vir}}$ relation still exhibits significant scatter, hints that there might be residual dependence of R_e on morphological type. It remains an interesting open question for future studies, whether additional halo properties can help tighten the relation between galaxy size and halo virial radius further.

9 CONCLUSION

In this paper, we use two suites of cosmological hydrodynamical simulations to study the correlation between galaxy spin and its host halo spin, and examine the relation between galaxy effective radius and halo virial radius. The two suites differ significantly in numerical resolution and in the strength of stellar feedback, yet show similar results regarding the correlation of spins and the galaxy size - halo size relation, from which we draw the following conclusions.

(i) The distribution of galaxy spin follow similar log-normal shapes to that of their host haloes. The median values differ for different components: the spin of stars within $0.1 R_{\text{vir}}$ has the value of ~ 0.005 - 0.007 , while the spin of cold gas within $0.1 R_{\text{vir}}$ is ~ 0.02 - 0.03 , slightly lower than but of the same order of the dark matter halo spin (~ 0.037), in qualitatively agreement with what is inferred from the H_α kinematics of massive star forming galaxies at high- z (Burkert et al. 2016).

(ii) The similarity of the spin distributions does not translate to a correlation between the spins of each given galaxy and the spins of its host halo. Both simulation suites show that galaxy spin λ_{gal} and host halo spin λ_{halo} are barely correlated, especially at $z \gtrsim 1$. This null correlation is qualitatively the same, if the spin of the galaxy is measured for the cold gas or the stars separately. There seems to be a weak correlation between λ_{gal} and λ_{halo} at $z \lesssim 1$. Given that the specific angular momentum of cold gas and dark matter are correlated at the accretion into the halo virial radius, this indicates that the gas angular momentum is not conserved during the gas inflow into the galaxy and its evolution within the galaxy. The spin of the inner part of the dark matter halo shows a correlation with that of the galaxy, but this is a consequence of baryonic effect on the dark matter halo, such that the inner halo spin from N -body simulations cannot serve as a proxy for the galaxy spin.

(iii) The angular momentum retention factor, f_j ($\equiv \lambda_{\text{gal}}/\lambda_{\text{halo}}$), has a value of ~ 0.5 on average, with large, stochastic variations from galaxy to galaxy and from one time to another, and it anti-correlates with λ_{halo} . Wet compaction or mergers could potentially give rise to the anti-correlation between f_j and λ_{halo} .

Low- λ_{halo} galaxies tend to develop a wet compaction (Dekel & Burkert 2014), which causes the initially low-spin system to end up with higher λ_{gas} by depleting the low-angular momentum gas in the compact star forming nucleus phase, and acquiring higher-angular momentum gas that settles in an extended ring. The merger of massive satellites causes λ_{halo} and λ_{gal} to rise and fall *in turn*, over a time scale of several halo dynamical times. Based on the picture of angular momentum gain and loss described in Danovich et al. (2015), we also speculated on other possible mechanisms, which do not necessarily cause an anti-correlation between f_j and λ_{halo} , but smear out the $\lambda_{\text{gal}}-\lambda_{\text{halo}}$ correlation.

(iv) Contrary to the uncorrelated spin amplitudes, the spin orientations of a galaxy and its host halo are correlated. Overall, half of the cases have $\cos\theta \gtrsim 0.6$, where θ is the angle between the galaxy spin vector and halo spin vector. At a given halo mass bin, the alignment becomes marginally weaker at later times. This suggests that the mechanisms that smear out the correlation of the amplitudes of spin do not totally randomize the alignment. The spin alignment is consistent with the finding that the inflow is predominantly in a preferred plane (Danovich et al. 2012), such that the torques exerted are preferentially along the spin vector, thus affecting its amplitude but not its direction.

(v) The NIHAO simulations, which have stronger stellar feedback than the VELA simulations, show a marginally stronger correlation between the spin of the galaxy and of its host halo, and a slightly better alignment between the spin vectors. This may suggest that stronger feedback operates to the advantage of a better correlation, via stronger angular momentum exchange between the inner part and outskirts of a galaxy. We caution though that this interpretation is hindered by the fact that NIHAO has poorer resolution, which, as with strong feedback, also reduces the clumpiness of galaxies and thus is disadvantageous to angular momentum exchange.

(vi) The spins of the cold gas and the stars in a galaxy are correlated, with $\mathcal{R} \sim 0.6 - 0.8$, strengthening at later times. The spin vectors of the baryonic components are well aligned, with about half of the cases having $\cos\theta_{\text{gas,star}} \gtrsim 0.97$. The alignment is better for more massive systems. A non-negligible fraction of the cases have counter-rotating gas and stars, especially in lower-mass systems.

(vii) We find that the halo spin parameter is not significantly correlated with galaxy size in both simulation suites, challenging the conventional, semi-analytic galaxy size estimator: $R_e \simeq 0.5\lambda_{\text{halo}}R_{\text{vir}}$. Nevertheless, both VELA and NIHAO reproduce the empirical relation derived from abundance matching, $R_e \simeq AR_{\text{vir}}$, with the proportionality factor $A \simeq 0.02$ at low- z and increasing towards high- z . We find that in the simulations, galaxy size can be well described by the relation

$$R_e = 0.02(c/10)^{-0.7}R_{\text{vir}} \quad (10)$$

where c is the halo concentration. The concentration dependence serves two purposes. First, at fixed halo mass and redshift, the size of individual galaxies anti-correlates with halo concentration as $c^{-0.7}$. Second,

there is a redshift dependence associated with the $c^{-0.7}$ factor, which comes in via the concentration-mass-redshift relation and accurately captures the redshift evolution of A in the simulations. This redshift trend, however, is too strong compared to that inferred from observation using abundance matching and a simplified deprojection of sizes, and thus seems to cause over-prediction of galaxy size at high redshift at given M_* . Although there might be some caveats that could potentially change the results deduced from observations, if reproducing the observed R_e-M_* relations across redshifts is the primary concern, one can apply an extra redshift dependence to the size predictor, making it $R_e = 0.02(1+z)^{-0.2}(c/10)^{-0.7}R_{\text{vir}}$. We clarify again that this is a deviation from eq. (10) that accurately describe the redshift dependence in the simulations, and should be adopted if the tension between the simulated sizes and the sizes deduced from observations at high redshift is confirmed to be valid. This will imply that the simulated radii are inaccurate at high redshift. Alternatively, one can assume that the tension is an artifact of the process of analyzing the simulations, that the simulations are reliable, and adopt eq. (10). The empirical relation can be tested with future observations where concentration and virial radius are measured from gravitational lensing. It remains an open question how the potential well of the host halo regulates the size of the galaxy to give rise to the specific $c^{-0.7}$ scaling.

ACKNOWLEDGMENTS

We acknowledge stimulating discussions with Andreas Burkert and Reinhard Genzel. This work was partly supported by the grants ISF 124/12, I-CORE Program of the PBC/ISF 1829/12, BSF 2014-273, PICS 2015-18, and NSF AST-1405962. FJ is supported by the Planning and Budgeting Committee (PBC) fellowship of the Council for Higher Education in Israel. JP is support by the grant HST-AR-14578.001-A. The VELA simulations were performed at the National Energy Research Scientific Computing Center (NERSC) at Lawrence Berkeley National Laboratory, and at NASA Advanced Supercomputing (NAS) at NASA Ames Research Center. DC is supported by the ERC Advanced Grant, STARLIGHT: Formation of the First Stars (project number 339177). The NIHAO simulations were performed on the High Performance Computing resources at New York University Abu Dhabi; on the THEO cluster of the Max-Planck-Institut für Astronomie and on the HYDRA clusters at the Rechenzentrum in Garching.

REFERENCES

- Barro G. et al., 2016, ApJ, 820, 120
- Barro G. et al., 2015a, arXiv:1509.00469
- Barro G. et al., 2013, ApJ, 765, 104
- Barro G. et al., 2014a, ApJ, 791, 52
- Barro G., Trump J., Koo D. C., Dekel A., Kassin S. A., Kocevski D., Faber S. M., Candel, 2015b, in

- American Astronomical Society Meeting Abstracts, Vol. 225, American Astronomical Society Meeting Abstracts, p. 111.07
- Barro G., Trump J. R., Koo D. C., Dekel A., Kassin S. A., Kocevski D. D., Faber S. M., et al., 2014b, arXiv:1405.7042
- Behroozi P. S., Wechsler R. H., Conroy C., 2013, ApJ, 57
- Benson A. J., 2012, *New Astronomy*, 17, 175
- Bett P., Eke V., Frenk C. S., Jenkins A., Helly J., Navarro J., 2007, MNRAS, 376, 215
- Bett P., Eke V., Frenk C. S., Jenkins A., Okamoto T., 2009, arXiv.org, 1137
- Blumenthal G. R., Faber S. M., Primack J. R., Rees M. J., 1984, *Nature*, 311, 517
- Bryan G. L., Norman M. L., 1998, ApJ, 495, 80
- Buck T., Macciò A. V., Obreja A., Dutton A. A., Domínguez-Tenreiro R., Granato G. L., 2017, MNRAS, 468, 3628
- Bullock J. S., Dekel A., Kolatt T. S., Kravtsov A. V., Klypin A. A., Porciani C., Primack J. R., 2001, ApJ, 555, 240
- Burkert A. et al., 2016, ApJ, 826, 214
- Ceverino D., Dekel A., Bournaud F., 2010, MNRAS, 404, 2151
- Ceverino D., Dekel A., Mandelker N., Bournaud F., Burkert A., Genzel R., Primack J., 2012, MNRAS, 420, 1005
- Ceverino D., Klypin A., 2009, ApJ, 695, 292
- Ceverino D., Klypin A., Klimek E. S., Trujillo-Gomez S., Churchill C. W., Primack J., Dekel A., 2014, MNRAS, 442, 1545
- Ceverino D., Primack J., Dekel A., 2015, MNRAS, 453, 408
- Chabrier G., 2003, PASP, 115, 763
- Collaboration P. et al., 2016, A&A, 594, A13
- Croft R. A. C., Di Matteo T., Springel V., Hernquist L., 2009, MNRAS, 400, 43
- Danovich M., Dekel A., Hahn O., Ceverino D., Primack J., 2015, MNRAS, 449, 2087
- Danovich M., Dekel A., Hahn O., Teyssier R., 2012, MNRAS, 422, 1732
- DeFelippis D., Genel S., Bryan G. L., Fall S. M., 2017, *The Astrophysical Journal*, 841, 16
- Dekel A., Burkert A., 2014, MNRAS, 438, 1870
- Dekel A., Krumholz M. R., 2013, MNRAS, 432, 455
- Dekel A., Sari R., Ceverino D., 2009, ApJ, 703, 785
- Doroshkevich A. G., 1970, *Astrofizika*, 6, 581
- Dunkley J. et al., 2009, ApJS, 180, 306
- Dutton A. A. et al., 2010, arXiv.org, 322
- Dutton A. A., Macciò A. V., 2014, MNRAS, 441, 3359
- Dutton A. A., Mendel J. T., Simard L., 2011, arXiv.org
- Fall S. M., Efstathiou G., 1980, MNRAS, 193, 189
- Genel S. et al., 2014, MNRAS, 445, 175
- Guo Q. et al., 2011, MNRAS, 413, 101
- Hahn O., Teyssier R., Carollo C. M., 2010, MNRAS, 405, 274
- Hearin A. P., Watson D. F., 2013, arXiv.org, 1313
- Huang K.-H. et al., 2017, arXiv.org
- Kaufmann T., Mayer L., Wadsley J., Stadel J., Moore B., 2006, arXiv.org, 53
- Kennicutt, Jr. R. C., 1998, ApJ, 498, 541
- Knollmann S. R., Knebe A., 2009, ApJS, 182, 608
- Kravtsov, 2013, ApJL, 764, L31
- Kravtsov A. V., 2003, ApJL, 590, L1
- Kravtsov A. V., Klypin A. A., Khokhlov A. M., 1997, ApJS, 111, 73
- Lange R. et al., 2015, MNRAS, 447, 2603
- Lee C. T., Primack J. R., Behroozi P., Rodríguez-Puebla A., Hellinger D., Dekel A., 2017a, MNRAS, 466, 3834
- Lee C. T., Primack J. R., Behroozi P., Rodríguez-Puebla A., Hellinger D., Dekel A., 2017b, arXiv.org
- Mo H. J., Mao S., White S. D. M., 1998, MNRAS, 295, 319
- Moster B. P., Naab T., White S. D. M., 2013, MNRAS, 428, 3121
- Muñoz-Cuartas J. C., Macciò A. V., Gottlöber S., Dutton A. A., 2011, MNRAS, 411, 584
- Navarro J. F., Frenk C. S., White S. D. M., 1997, ApJ, 490, 493
- Peebles P. J. E., 1969, ApJ, 155, 393
- Porciani C., Dekel A., Hoffman Y., 2002a, MNRAS, 332, 325
- Porciani C., Dekel A., Hoffman Y., 2002b, MNRAS, 332, 339
- Rodríguez-Gomez V. et al., 2017, MNRAS, 467, 3083
- Sharma S., Steinmetz M., Bland-Hawthorn J., 2012, *The ApJ*, 750, 107
- Shen S., Wadsley J., Stinson G., 2010, MNRAS, 407, 1581
- Somerville R. S. et al., 2018, MNRAS, 473, 2714
- Somerville R. S., Hopkins P. F., Cox T. J., Robertson B. E., Hernquist L., 2008, MNRAS, 391, 481
- Stinson G., Seth A., Katz N., Wadsley J., Governato F., Quinn T., 2006, MNRAS, 373, 1074
- Stinson G. S. et al., 2013, MNRAS, 436, 625
- Tacchella S., Dekel A., Carollo C. M., Ceverino D., DeGraf C., Lapiner S., Mandelker N., Primack J. R., 2016, MNRAS, 458, 242
- Teklu A. F., Remus R.-S., Dolag K., Beck A. M., Burkert A., Schmidt A. S., Schulze F., Steinborn L. K., 2015, *The ApJ*, 812, 29
- Tomassetti M. et al., 2016, MNRAS, 458, 4477
- van der Wel A. et al., 2014, ApJ, 788, 28
- Wadsley J. W., Keller B. W., Quinn T. R., 2017, MNRAS, 471, 2357
- Wadsley J. W., Veeravalli G., Couchman H. M. P., 2008, MNRAS, 387, 427
- Wang L., Dutton A. A., Stinson G. S., Macciò A. V., Penzo C., Kang X., Keller B. W., Wadsley J., 2015, MNRAS, 454, 83
- Wechsler R. H., Bullock J. S., Primack J. R., Kravtsov A. V., Dekel A., 2002, ApJ, 568, 52
- White S. D. M., 1984, ApJ, 286, 38
- White S. D. M., Rees M. J., 1978, MNRAS, 183, 341
- Zavala J. et al., 2016, MNRAS, 460, 4466
- Zhao D. H., Jing Y. P., Mo H. J., Börner G., 2009, ApJ, 707, 354
- Zjupa J., Springel V., 2017, MNRAS, 466, 1625
- Zolotov A. et al., 2015, MNRAS, 450, 2327

APPENDIX A: HALO CONCENTRATION MEASUREMENT

We measure the halo concentration parameter by fitting the circular velocity profile $V_c(r) = \sqrt{GM_{\text{dm}}(<r)}/r$ of the simulated galaxies with an NFW profile, where $M_{\text{dm}}(<r)$ is the dark matter mass within radius r . The circular velocity profile is measured in 30 spherical shells with equal thickness in logarithmic scale between $0.01-1R_{\text{vir}}$. In practice, we minimize the following figure of merit:

$$\text{RMS}^2 = \frac{1}{N} \sum_{i=1}^{N=30} \left[\frac{V_{c,\text{NFW}}(x_i | M_{\text{vir}}, c) - V_c(x_i)}{V_c(x_i)} \right]^2 \quad (\text{A1})$$

where

$$V_{c,\text{NFW}}(x | M_{\text{vir}}, c) = \sqrt{G \frac{M_{\text{vir}}}{r} \frac{f(cx)}{f(c)}}, \quad (\text{A2})$$

with $f(y) = \ln(1+y) - y/(1+y)$ and $x = r/R_{\text{vir}}$.

Note that for Fig. 12 and Fig. 13, we have excluded the snapshots with $\text{RMS} > 0.07$, corresponding to the worst 20% fits, where the NFW profile is not a good description of the dark matter halo density profile. Usually the excluded cases are associated with major mergers.

APPENDIX B: CONCENTRATION DEPENDENCE AT FIXED HALO MASS AND REDSHIFT

Here we illustrate that, at fixed halo mass and redshift, galaxy size anti-correlates with halo concentration in our simulations.

Fig. B1 shows the ratio R_e/R_{vir} versus λ_{halo} and c , for simulated galaxies in a small range of halo mass and redshift. For individual galaxies (snapshots), the ratio R_e/R_{vir} depends on halo concentration c , the trend of which is well described by $c^{-0.7}$; and does not depend on λ_{halo} , in both VELA and NIHAO. The qualitative trend is valid no matter the halo properties (c , λ_{halo} , and R_{vir}) are measured from the matching dark-matter-only runs of the NIHAO suite or in the fiducial hydro simulations.⁹ Further ensuring that the c -dependence is not a mass trend or redshift trend, we have verified that in narrow ranges of M_{vir} and c , the ratio R_e/R_{vir} does not depend on z , and that in narrow ranges of z and c , the ratio R_e/R_{vir} does not depend on M_{vir} .

APPENDIX C: COMPARISON OF THE MEDIAN SIZE-MASS RELATIONS

In the new galaxy size predictor as given by $R_e = 0.02(c/10)^{-0.7}R_{\text{vir}}$, there are two roles of the concentration dependence. Here we illustrate one of them, that

⁹ The data points are sparser in the DMO panels than in the hydro panels, because the output timesteps are thicker: for every 4 hydro outputs, there is one DMO output.

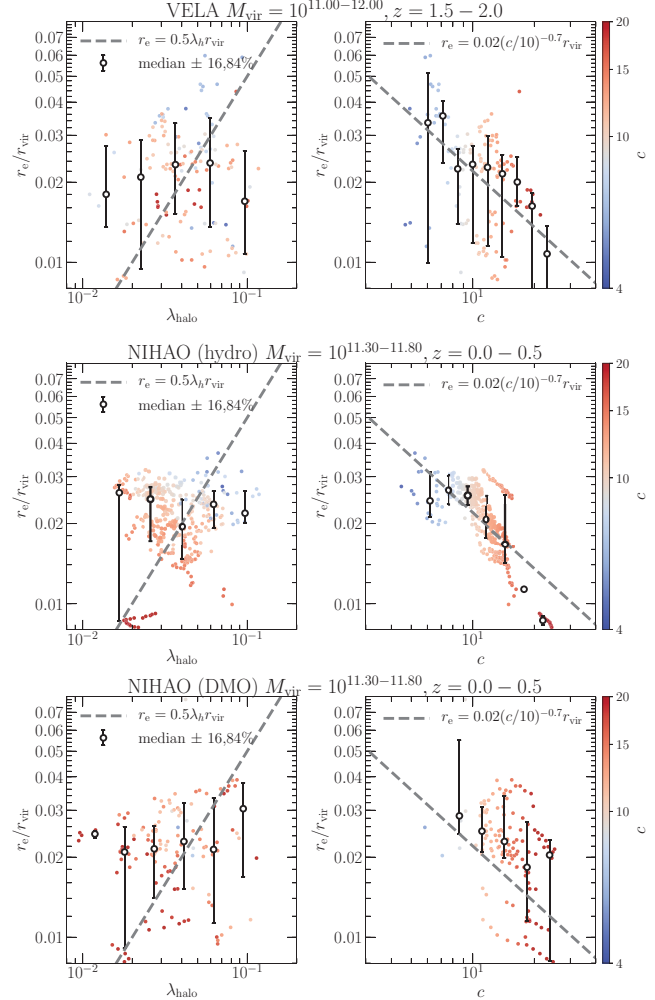


Figure B1. The ratio R_e/R_{vir} as a function of spin λ_{halo} (left) and concentration c (right), in a narrow range of halo mass and redshift. *Top* : VELA galaxies with $M_{\text{vir}} = 10^{11-12} M_{\odot}$ at $z = 1.5 - 2$. *Middle* : NIHAO galaxies with $M_{\text{vir}} = 10^{11.3-11.8} M_{\odot}$ at $z = 0 - 0.5$. *Bottom* : NIHAO galaxies with $M_{\text{vir}} = 10^{11.3-11.8} M_{\odot}$ at $z = 0 - 0.5$, with galaxy size measured from the fiducial hydro simulation, and halo properties measured from the matching dark-matter-only simulations. The dashed reference lines represent $R_e = 0.5\lambda_{\text{halo}}R_{\text{vir}}$ and $R_e = 0.02(c/10)^{-0.7}R_{\text{vir}}$, as indicated. The three rows all show: In a narrow range of redshift and halo mass, the ratio R_e/R_{vir} is clearly dependent on halo concentration c , well described by $c^{-0.7}$ and almost independent of halo spin λ_{halo} .

the average R_e - R_{vir} relation evolves with redshift, and the redshift dependence as found in the simulations is well described by $c^{-0.7}$ through the concentration-mass-redshift relation. In Appendix B, we illustrate the other role that, at fixed redshift and halo mass, the size of individual galaxies in the simulations anti-correlates with c , and is well described by $c^{-0.7}$.

Fig. C1 shows the ratio $A(z)$ between the median galaxy size $\langle R_e \rangle$ and the median halo virial radius $\langle R_{\text{vir}} \rangle$ as a function of redshift z . In our simulations, $A(z)$ increases by more than a factor of 2 from $z = 0$ to $z = 3$. Using the concentration-mass-redshift relation

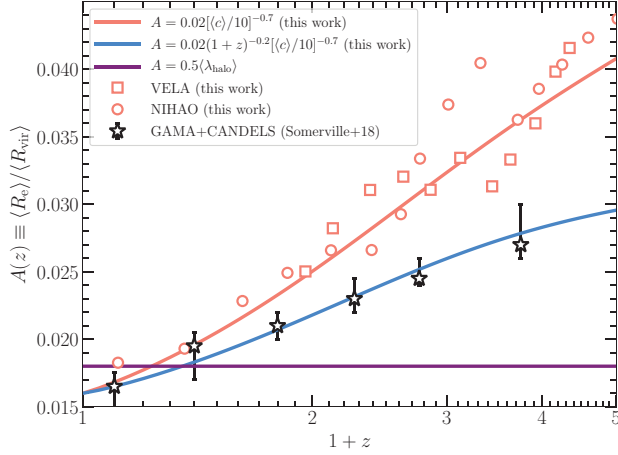


Figure C1. The zero-point of the median galaxy size - halo radius relation, $A(z) \equiv \langle R_e \rangle / \langle R_{\text{vir}} \rangle$, as a function of redshift z . The orange line represents the model proposed in this work, i.e., $A(z) = 0.02[\langle c \rangle (M_{\text{vir}}(z)/10)]^{-0.7}$, where $\langle c \rangle$ is given by the median concentration-mass-redshift relation of Dutton & Macciò (2014), and we adopt $M_{\text{vir}} = 10^{11} M_{\odot}$, a typical halo mass in our simulations, for illustration. The squares and circles represent the VELA and NIHAO results, respectively. Note that for the simulation results, we have scaled the overall normalization up and down slightly just to align them roughly to better reveal the redshift trend. The black stars represent observations (abundance matching) adopted from Somerville et al. (2018), for galaxies with $M_{*} < 10^{10.5} M_{\odot}$, with the errorbars indicate the full uncertainty in $\langle R_e \rangle / \langle R_{\text{vir}} \rangle$. The blue line represents $A(z) = 0.02(1+z)^{-0.2}[\langle c \rangle (M_{\text{vir}}(z)/10)]^{-0.7}$. The purple line represents $A = 0.5\langle \lambda_{\text{halo}} \rangle$, with $\langle \lambda_{\text{halo}} \rangle = 0.036$, assuming that $\langle \lambda_{\text{halo}} \rangle$ does not evolve with redshift. Obviously, the factor $c^{-0.7}$ introduces a z -dependence that matches the simulation results well but is steeper than that inferred from abundance matching. To enforce an agreement with the abundance matching result, an extra z -dependence of $(1+z)^{-0.2}$ is required.

from Dutton & Macciò (2014), we find that $A \propto c^{-0.7}$ nicely captures this behavior.

Observationally, however, the z -dependence is weaker: applying halo abundance matching to galaxies from the GAMA survey and the CANDELS survey, Somerville et al. (2018) find that A increases by about 60% from $z = 0.1$ to $z = 2.75$. This is illustrated in Fig. C1 with the black stars. Obviously, the $c^{-0.7}$ factor that well describes the z -dependence of the simulations overpredicts the z -dependence of the observational (abundance matching) R_e - R_{vir} relations. Therefore, if the relation $R_e = 0.02(c/10)^{-0.7} R_{\text{vir}}$ is used in a semi-analytic or semi-empirical model, the model will not pass a key benchmark test – the galaxy size-mass relation.

That said, if a perfect reproduction of the z -trend is needed, one can introduce empirically an extra z -dependence in the size predictor:

$$R_e = f(z) [\langle c \rangle (M_{\text{vir}}(z)/10)]^{-0.7} R_{\text{vir}}. \quad (\text{C1})$$

We find that with $f(z) = 0.02(1+z)^{-0.2}$, eq. (C1) reproduces the observationally deduced results quite well. This can also be seen in Fig. C1.

We emphasize that the c -dependence is introduced not only to reproduce the average z -dependence, but also to capture the c -dependence of the size of individual galaxies at fixed halo mass and redshift, in our simulations (Appendix B). The $f(z)$ factor needed may reflect intrinsic inconsistencies between the simulations and observations.